ABSTRACT

Title of Document: DEVELOPMENT OF SINGLE-MOLECULE FORCE AND TORQUE MEASUREMENT WITH APPLICATION TO NUCLEOSOME DISRUPTION.

Jen-Chien Chang, Doctor of Philosophy, 2014

Directed By: Assistant Professor Arthur La Porta, Department of Physics

Single-molecule force spectroscopy is a powerful method in biophysical research. The ability of detecting and manipulating single molecule finds applications in studies from DNA to cell, leads to various mechanism-based results. Among many tools in this field, optical traps is suitable for studies involving nucleic acids and its interaction with protein due to the high temporal and spatial resolution. While most experiments characterize force and displacement, the quest for manipulating and detecting torque and angular motion is increasing due to their significant role in many biological processes. This thesis mainly devotes to the development and application of an optical torque wrench which is capable of simultaneously controlling and measuring force, displacement, torque, and angular displacement of a single bio-molecule. First, angular manipulation of oblate polystyrene particles is demonstrated. Moreover, a new method for fabricating birefringent nanocylinders via nanosphere lithography is presented. Both particles are shown to provide stable angular trapping

in a home-built optical torque wrench. We then apply them in measuring a single DNA molecule under force and torque. Mechanical stability of nucleosome under tension and torsion is also studied, followed by a theoretical model to elucidate the importance of torsion in such experiments. Finally, the effect of experimental parameters in a surface-based optical traps on measured kinetics of bio-molecule is detailed.

DEVELOPMENT OF SINGLE-MOLECULE FORCE AND TORQUE MEASUREMENT WITH APPLICATION TO NUCLEOSOME DISRUPTION.

By

Jen-Chien Chang

Dissertation submitted to the Faculty of the Graduate School of the
University of Maryland, College Park, in partial fulfillment
of the requirements for the degree of
Doctor of Philosophy
2014

Advisory Committee:
Assistant Professor Arthur La Porta, Chair
Professor Christopher Jarzynski
Associate Professor Wolfgang Losert
Associate Professor Garegin Papoian
Assistant Professor Arpita Upadhyaya

Acknowledgements

First and foremost, I would like to thank my advisor, Professor Arthur La Porta, whose inspiration, guidance, and support are essential for all works in the thesis. I also thank my advisory committees for reviewing the manuscript and other professors who educated and mentored me. I especially thank my colleague Dr. Michel de Messières. Discussions with him constitute the backbone of many projects. I thank Barbara Brawn-Cinani and other lab members for helps in need. I acknowledge Ping-Chun Li, Professor Edward Yu, and the Studitsky Lab, whose collaboration contributes greatly to the work presented in this thesis. I also appreciate all outstanding scholars I met in the past six years who inspired me during scientific discussions.

I owe my deepest thank to my roommates Andrew Chen, Che-Yu Chen, Ming-Jer Lee, Guo-Yuan Lien, Tung-Chang Liu, Wei-Hsuan Yu's family, and other friends I made here as well as in Taiwan. Special thanks are given to Weichun Fong and Chen-Hsiang Hung. Life as a foreign student can be challenging without their warmest supports. Those good times with them are my invaluable resources in the future.

Last but not least, I am grateful to my family for their sacrifice and company. Words cannot express my sincerest gratitude.

Table of Contents

List of Tables

List of Figures

Chapter 1: Introduction to Single-Molecule Experiments Using Optical Traps

1.1 Outline of Thesis

This thesis explores the development of optical traps and its improved version (termed optical torque wrench (OTW)) for force and torque measurements as well as the application to biophysical experiments at single-molecule level. In the first chapter, single molecule experiment with optical traps is introduced. The principle, instrumentation, and calibration of optical traps are reviewed, followed by applications to energy landscape reconstruction, dynamic force spectroscopy, and tracking dynamics of transcribing RNA polymerase. Chapter two details the construction of an optical torque wrench and an application to measure the mechanical response of single DNA molecule under rotation. Chapter three describes a research of mechanical stability of single nucleosome subject to tension and torsion. Both experiments conducted using optical torque wrench and theoretical models are summarized. Chapter four is a detailed research about how the measured kinetics affected by experimental parameters in the surface-based optical traps. Finally, summaries and future directions conclude the thesis.

1.2 Single-Molecule Experiments

Structure and function are closely related in biological systems of all scales. Following the evolution of detailed molecular structures over time can lead to the discovery of underlying mechanisms behind biological processes. However it would require synchronizing all molecular trajectories in time, which is difficult in traditional bulk biochemical assays. Ensemble studies also tend to mask rare but potentially important events. Moreover, even if no dynamical processes are involved, observation obtained from averaging over population can be misleading if the distribution of states is multimodal [1].

One solution is to track one molecule at a time. Upon measuring many single molecules, a histogram of observables is established instead of only average values. The major challenge in this methodology is to detect a tiny signal on a molecular scale. Many tools have been developed in the past two decades to overcome this difficulty [2]. Single-molecule detection is one approach [3]. For example, a molecule can be tagged with a pair of fluorescent labels that undergoes fluorescent resonance energy transfer (FRET) when they are in close proximity, and conformation changes of the molecule is tracked by detecting the FRET signal. On the other hand, in single-molecule manipulation method [4], the molecule is usually attached to an probe which is held by external optical or magnetic field. Controlling and monitoring such a probe allow us to obtain dynamic information of the molecule as well as the response to force perturbation.

Among many single-molecule techniques, optical traps (or optical tweezers) have been used to characterize various bio-molecules and biological processes in

measurements of force and displacement in picoNewton and sub-nanometer regime. In this chapter, we will first review the principle, instrumentation, and calibration of optical traps, which forms the basis for this thesis. Experiments conducted using optical traps in our laboratory are then summarized.

1.3 Optical Traps

1.3.1 Principle

Optical trapping has grown into an active research field with many applications since the first demonstration of Ashkin [5,6]. An optical trap is essentially a tightly focused Gaussian laser beam created with an objective lens of high numeric aperture such that a dielectric particle can be trapped near the focus. Figure 1.1 shows for both axial and lateral direction, a stably trapped dielectric microsphere feels restoring force when it is off the trapping center which is slightly above the laser focus. The simple explanation for this phenomenon is that the conservation of momentum demands the microsphere to have equal magnitude but opposite direction of momentum change with the scattered laser beam.

There are two limiting case where the optical force on a microsphere can be theoretically calculated [7]. When the radius of microsphere is much larger than the wavelength of laser, Mie scattering theory may be applied, i.e. the optical force can be computed from ray optics. On the other hand, if the radius of microsphere is much smaller than the wavelength of laser, the condition for Rayleigh scattering area satisfied and the microsphere can be treated as a point dipole. However, the microsphere in our application (~500 nm – 2 μm) usually has similar dimension with

the laser wavelength (1064 nm). A more rigorous electromagnetic theory is necessary for an accurate description. Recently, a toolbox based on Generalized Lorentz-Mie Theory has been developed to predict trapping efficiency for microspheres of a range of sizes and index of refractions [8]. In practice, the change of outgoing beam is measured by a position sensitive detector and calibration methods described in the following section are applied to characterize the force in experiments.

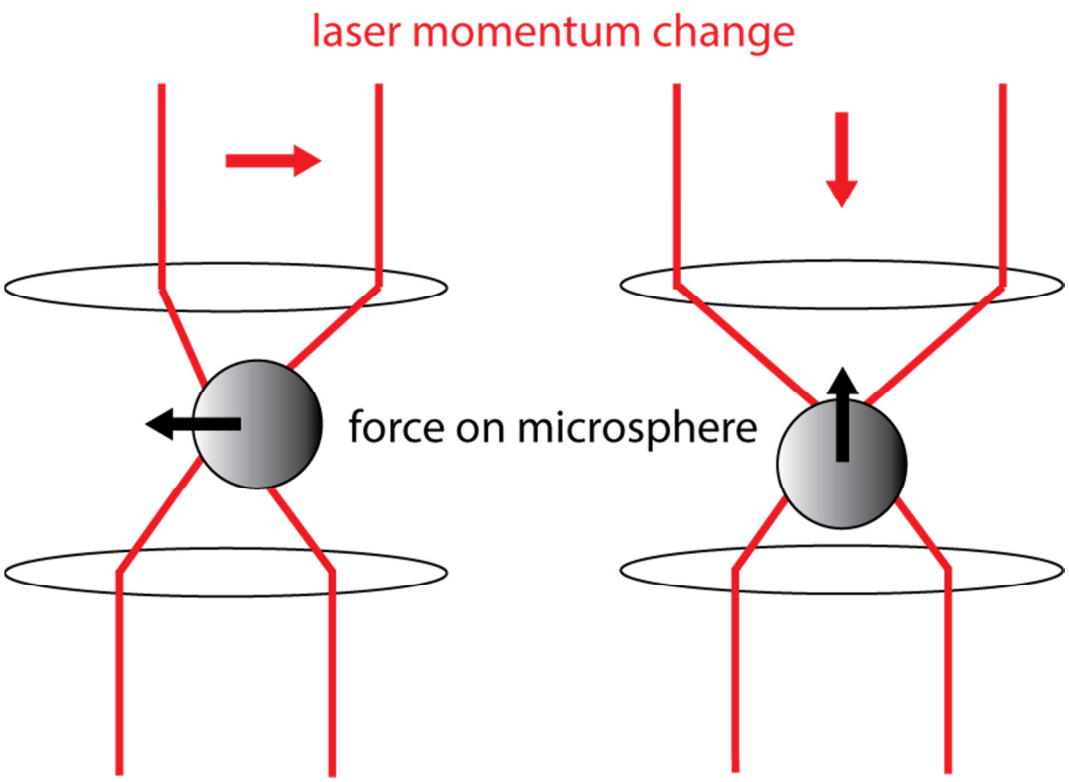

Figure 1.1: Principle of optical trapping. The microsphere is trapped at the center of a sharply focused laser beam due to requirement of momentum conservation. Momentum change of the laser beam and the microsphere must have equal magnitude but opposite direction, resulting a restoring force toward the trapping center of the laser beam.

1.3.2 Mechanical Design

The construction of optical traps is a major part of the study and the basis for development of further angular manipulation and torque measurement. Although basic optical traps only requires an objective of high NA value, more components are necessary for accurate laser alignment, steering, intensity control as well as measurement for force and displacement [9].

Figure 1.2 shows the schematics of our design which is constructed on a gas-suspended optical table for stability. A polarized infrared Nd:YAG laser (1064 nm, BL-106C, Spectra-Physics, Santa Clara, CA) is coupled into a single-mode, polarization-preserved optical fiber (Thorlabs, Newton, NJ) after passing through an acousto-optic modulator (AOM, Isomet, Springfield, VA) for intensity control. The coupling of a fiber makes the instabilities from laser power, mode, and pointing into the only intensity fluctuation of output beam which can be controlled feedback by AOM. The boxed region is constructed on a vertical optical table for convenient operation with sample loading. About 10% of light is diverged to an input detector for power monitoring. The other beam is aligned to the center of an oil immersion objective (NA 1.49, CFI Apo TIRF 100x, Nikon Instruments, Lewisville, TX) and oil immersion condenser (NA 1.4, Nikon Instrument). A sample chamber between the objective and condenser is mounted on a piezo stage (Physik Instrumente, Germany) for position control with nanometer resolution.

Light exiting condenser is collected and projected on a dual-axis position sensitive diode (PSD, DL100-7PCBA3, Pacific Silicon Sensor, Westlake Village, CA) with home-made amplifying circuit. As shown in Figure 1.1, relative position of microsphere to the trapping center can be tracked by monitoring beam deflection

using PSD. Axial sensitivity is possible by clipping the beam with an iris, which catches the broadening and narrowing of the beam. The analog signal is filtered using a 9-pole Bessel filter (Krohn-Hite, Brockton, MA) and collected on a 16-bit digital acquisition board (National Instrument, Austin, TX)

Another optical path using light emitting diode (532nm, Thorlabs, Newton, NJ) images the microsphere into a CCD camera for visualization and sample searching for experiments.

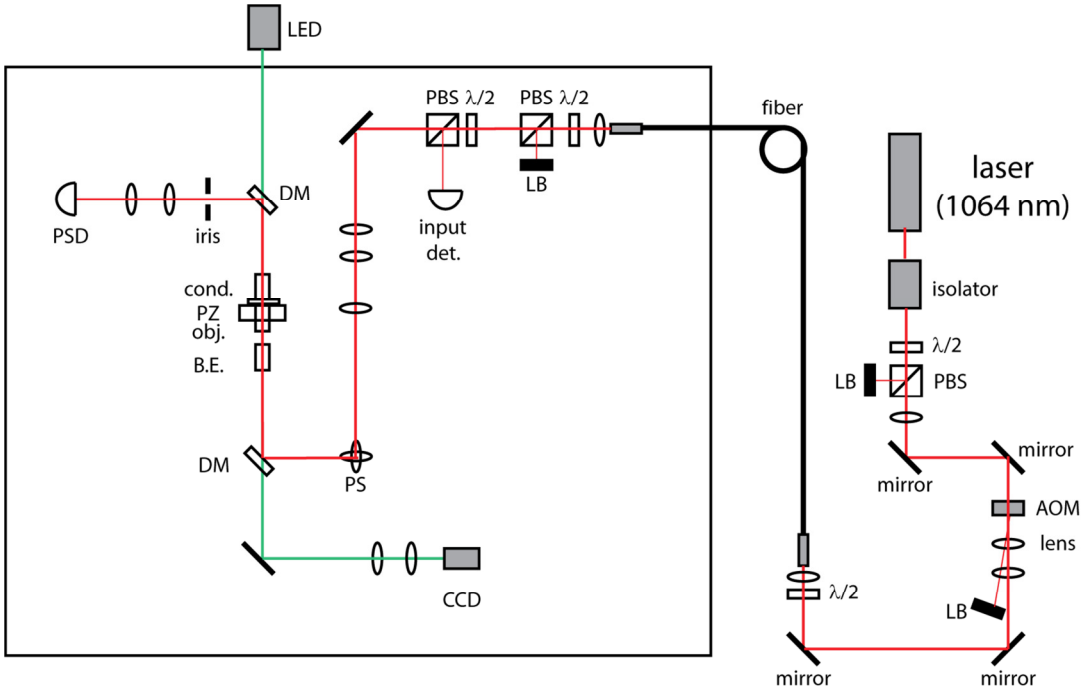

Figure 1.2: Schematic diagram for our home-built optical traps. LB: laser block. λ/2: half-wave plate. PBS: polarizing beam splitter. DM: dichroic mirror. cond: condenser. PZ: piezo stage. B.E.: beam expander. PSD: position sensitive detector.

1.3.3 Calibration

In order to convert the voltage measured by PSD to physical unit of force and displacement, there are numbers of method for calibration [4,9–12]. The methods we applied are described here. The Z-axis is defined as the axial direction of laser propagation, and x-axis and y-axis are the orthogonal lateral directions. The PSD measures deflection of laser in x and y direction, giving corresponding voltage signal V_x, V_y, and the total intensity V_{sum}. Z signal V_z is the normalized intensity V_{sum}/V_{input} where V_{input} is given by a separate input detector (Figure 1.2).

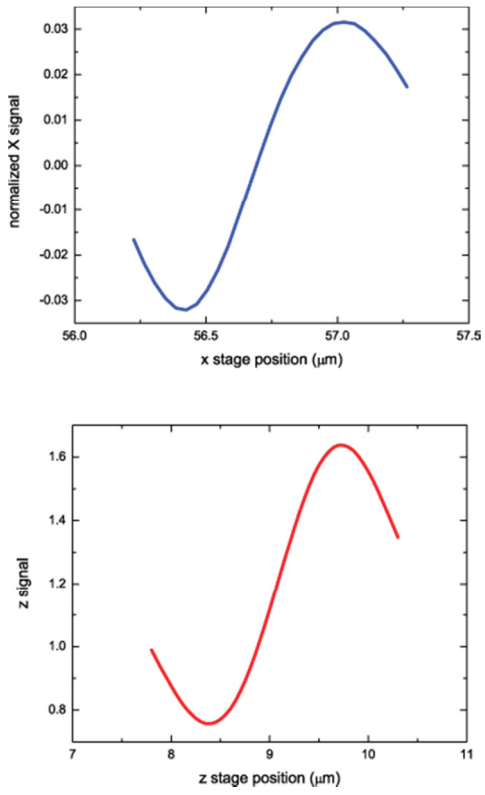

Figure 1.3: Example of position calibration in both x and z direction for a polystyrene microsphere of diameter 820 nm. Signals are recorded while the fixed microsphere is scanned across the center of laser trapping center.

Position calibration is accomplished by moving a microsphere across the center of laser beam. The microsphere is fixed to the surface of sample chamber (in 100 mM KCl and 10 mM sodium acetate pH 4.5 for help with immobilization) which can be moved by a piezo stage. The voltage on PSD as a function of position of the bead relative to trap center is recorded. Size variation of the microsphere is average by measuring many of them. Figure 1.3 shows an example of a polystyrene microsphere of diameter 820 nm scanned in x and z direction. Note that the signal is sensitive to the displacement of microsphere for about 1 μm in both x and z direction, and it is linear for small displacement.

Standard method for force calibration utilizes the power spectrum of Brownian motion for a freely trapped microsphere. We describe the physics here as it is also important for the torque calibration discussed in chapter 2. Considering a microsphere subject to thermal motion in a harmonic potential, for an environment with low Reynolds number the equation of motion in x direction can be written as

$$\alpha x(t) + \gamma \dot{x}(t) = F(t) \qquad (1.1)$$

where α is the trap stiffness, γ is the viscous drag, and $F(t)$ is the stochastic (Langevin) force. The equation in frequency space can be obtained by Fourier transform.

$$\alpha \tilde{x}(\omega) + i\omega\gamma \tilde{x}(\omega) = \tilde{F}(\omega) \qquad (1.2)$$

After rearrangement, the power spectrum of x fluctuation can be calculated.

$$|\tilde{x}(\omega)|^2 = \frac{\tilde{F}(\omega)^2}{\alpha^2 + \gamma^2\omega^2} \qquad (1.3)$$

For Brownian motion, the stochastic force has white frequency spectrum due to the vanishing correlation time, which can be set to a constant and determined by

integrating $\tilde{\boldsymbol{x}}(\boldsymbol{\omega})$. By the Equipartition Theorem, the microsphere will have energy $\boldsymbol{k_B T/2}$ in a 1-d harmonic potential. We obtain

$$\frac{1}{2}\alpha\langle x^2\rangle = \frac{1}{2}k_B T \qquad (1.4)$$

Therefore we can calculate $\langle x^2\rangle$

$$\langle x^2\rangle = \int_0^\infty |\tilde{x}(\omega)|^2\, d\omega = \frac{\pi\tilde{F}^2}{2\alpha\gamma} = \frac{k_B T}{\alpha} \qquad (1.5)$$

The constant $\tilde{F}^2 = 2\, k_B T\gamma/\pi$ is obtained. The power spectrum now can be written as

$$|\tilde{x}(\omega)|^2 = \frac{2k_B T\gamma/\pi}{\alpha^2 + \gamma^2\omega^2} \qquad (1.6)$$

or

$$S_x(f) = |\tilde{x}(f)|^2 = \frac{k_B T/\pi^2\gamma}{\left(\frac{\alpha}{2\gamma\pi}\right)^2 + f^2} = \frac{A^2}{f_0^2 + f^2} \qquad (1.7)$$

The power spectral density $S_x(f)$ has a squared Lorentzian form which is measurable. As shown in Figure 1.4, we are now able to fit the measured power spectrum to determine trap stiffness α in unit of pN/nm and drag γ in both x and z direction independently. Combined with position calibration which gives sensitivity in unit of nm/V, the voltage signal can be converted to physical unit of force in pN.

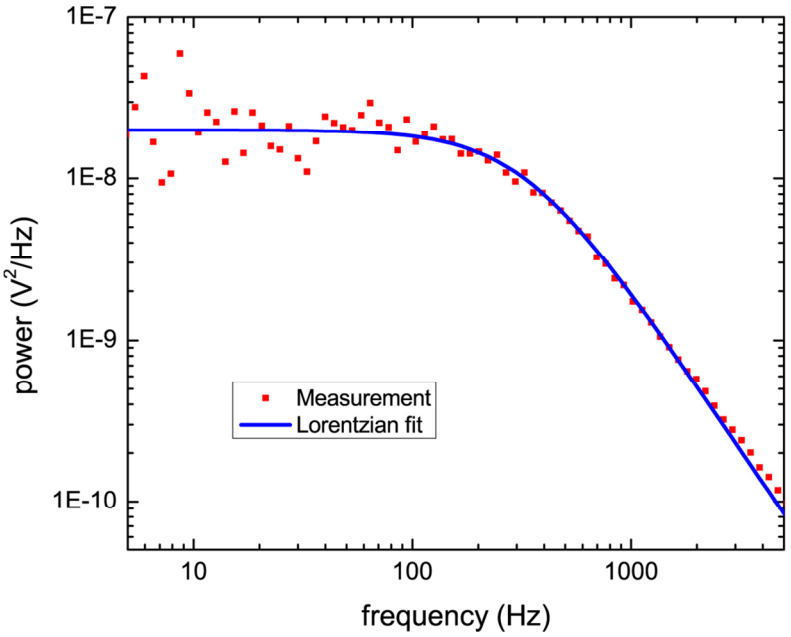

Figure 1.4: Calibration of force is achieved by measuring the power spectrum of Brownian fluctuation for a trapped microsphere. Example data for a polystyrene microsphere of 820 nm diameter is shown in red. A Lorentzian line fit (blue) gives roll-off frequency 320 Hz.

1.4 Applications of Optical Traps

In this section, applications of optical traps to single-molecule experiments are introduced. One typical experimental setup is shown in Figure 1.5. The target molecule (usually DNA or RNA with secondary structure of interest) annealed between two handle DNA is attached to a microsphere and surface by biotin and digoxigenin label respectively. The force is exerted on the molecule by bringing the surface down with piezo stage to disrupt the structure of interest while the force and total extension of molecule and DNA handle are recorded as a function of time. Force and extension curve is the raw data from which different analyzing method and technique can be applied to extract information about the molecule of interest.

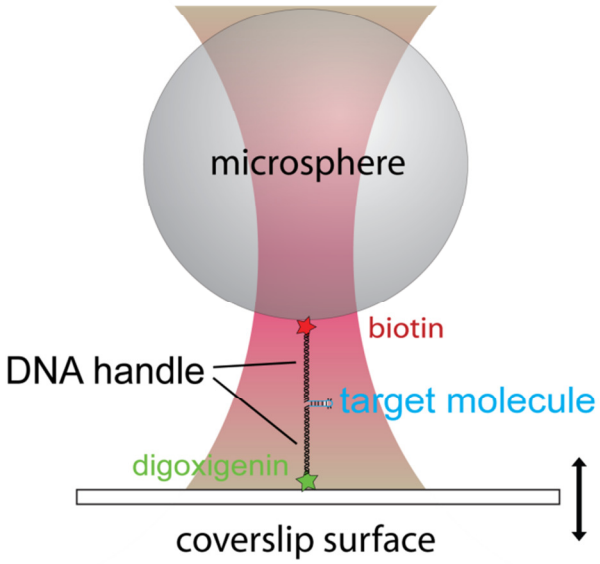

Figure 1.5: A typical surface-based setup for single-molecule experiments using optical traps (not to scale). The molecule of interest is disrupted by moving the coverslip surface down while the force and extension are recorded by detecting position of microsphere relative to the trap center.

1.4.1 Energy Landscape Reconstruction

In a disruption experiment shown above, the end to end distance (opening) of target construct can be calculated by subtracting the length of DNA handle from the total extension using worm like chain (WLC) theory [13]. This information is used in reconstructing energy landscape for an unfolding/folding transition of bio-molecule.

The technique for energy landscape reconstruction was first achieved by a constant force method [14,15]. However, the molecule in this scheme rarely populates transition state. We have developed an analyzing method where the energy landscape can be reconstructed for harmonically trapped biopolymer [16,17] which facilitate more rapid measurement with better statistics near transition barrier.

An intermediate step of calculating slope of the energy landscape *dE/dx* may be applied to characterizing bio-molecule. As shown in Figure 1.6, we disrupt -1 PRF (programmed ribosomal frameshifting) element of the CCR5 mRNA with optical trap. CCR5 mRNA promotes frameshifting in HeLa cells and its structure is the key to understanding the physical underpinnings of -1 PRF. The disruption of the structure in our experiment is an approximation of the process by which the ribosome disrupts the structure as it pulls the mRNA into its active site, so the measured unfolding energy should be indicative of the energy barrier encountered by the ribosome.

Four distinct disrupting pathways are observed as labeled by colors in Figure 1.6 by classifying *dE/dx* density plot. In principle, these might represent different disruption pathways of a common structure, or disruption pathways for different initial structure. By varying the relaxation time and measuring the occupancies of the conformations, it is evident that the different disruption pathways reflect different initial conformations (Figure 1.7). Combined with computational prediction, we have identified the blue pathway is consistent with a pseudoknot structure, green is the folding intermediate, and the red is a persistent alternate conformation. The strong resistance to disruption of the pseudoknot structure as well as the fact that the mRNA sequence can occupy an ensemble of relatively stable conformations may be important for the frameshifting mechanism.

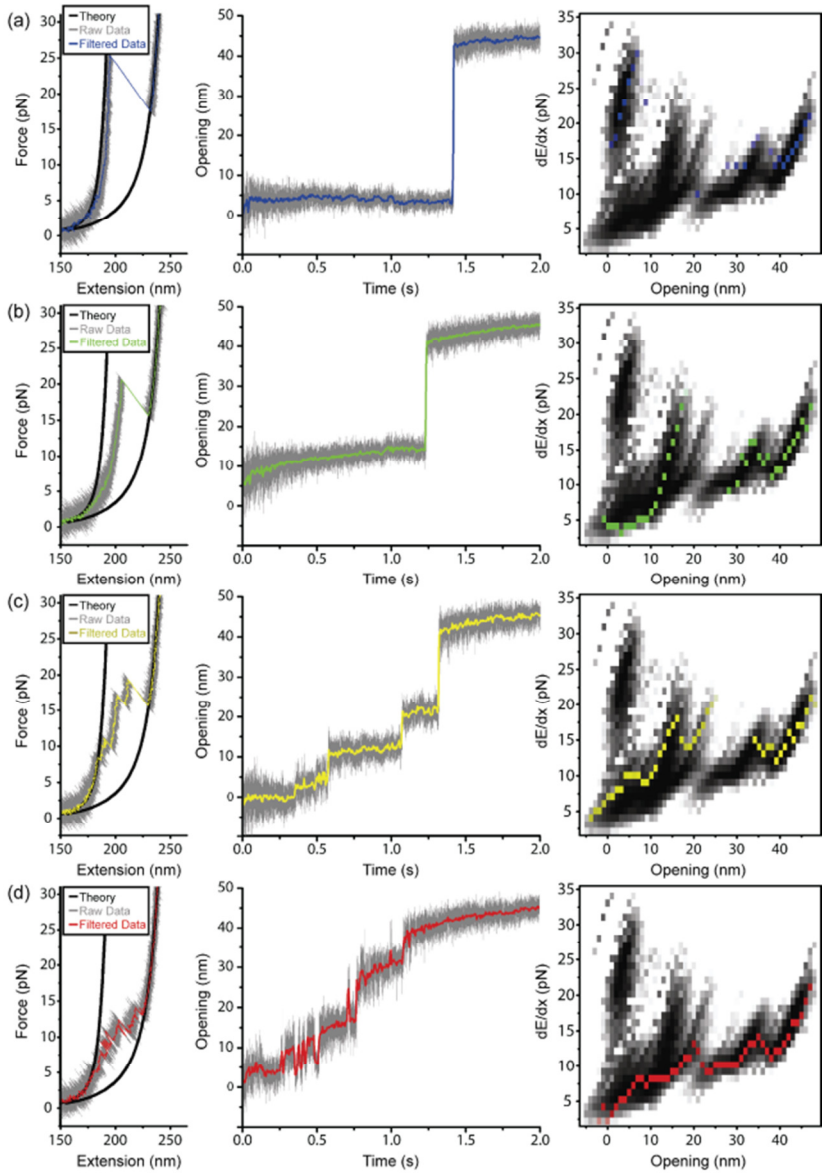

Figure 1.6: Example scans of CCR5 mRNA. Extension represents the combined length of the single-stranded RNA and hybrid DNA/RNA handles. Black lines: Worm-like chain theory for hybrid DNA/RNA handles with and without 97 additional bases of extended single-stranded RNA. Opening-time graphs show the same data as the force-extension plots where opening represents the end-to-end distance of the single-stranded RNA. Change in energy per opening distance (*dE/dx*) calculated as described previously. Gray scale density plot: The accumulated *dE/dx* probability density from all scans plotted on a log scale. Colored squares: *dE/dx* calculated for the single scan shown in the force-extension graph and opening-time graph.

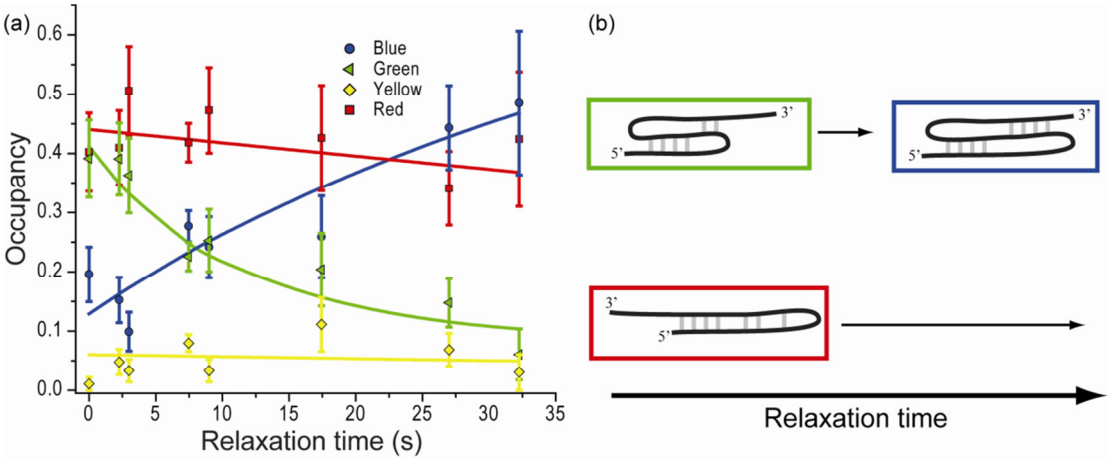

Figure 1.7: (a) Folding kinetics of the four conformations. The CCR5 mRNA structure was relaxed at 0 force for the specified time and the distribution of the four conformations was measured. Data was fit with exponential decay functions as a visual guide. (b) A cartoon illustrating the proposed folding pathway. The red state is stable, but a pseudoknot incorporating the 5' portion of the sequence (green) is replaced by a pseudoknot (blue) incorporating the full sequence.

Another application of energy landscape reconstruction technique is studying base-pair hybridization energies of nucleic acids, for instance, the DNA mismatch pair. The DNA mismatch repair system (MMR) is a critical pathway by which cells maintain the integrity of the genome. Dysfunction in the MMR mechanisms can directly induce cancer, so increased understanding of MMR may lead to therapeutic methods to treat disease. In Figure 1.8, we directly measure the binding energy of tandem GA mismatches (GA/AG) which are frequently bypassed by the MMR. We also studied three control sequences with no mismatches (TA/AT, GC/CG, and GA/CT). The four hairpins were identical except for two bases in the middle of the stem that were modified for study. The dE/dx plot shows the measured energy for

each hairpin while lines indicate a theoretically predicted model from MFold. Our results demonstrate that the GA/AG mismatch has significantly higher energy than would be expected if the GA mismatch was simply an open loop. This is presumably related to the reason the MMR misses GA mismatches. We also demonstrate that a single base change can be accurately measured at the single molecule level. This application demonstrates that single-molecule techniques can potentially replace bulk assays to precisely determine all possible combinations of binding energies, which would extend libraries used in structure predicting programs like MFold.

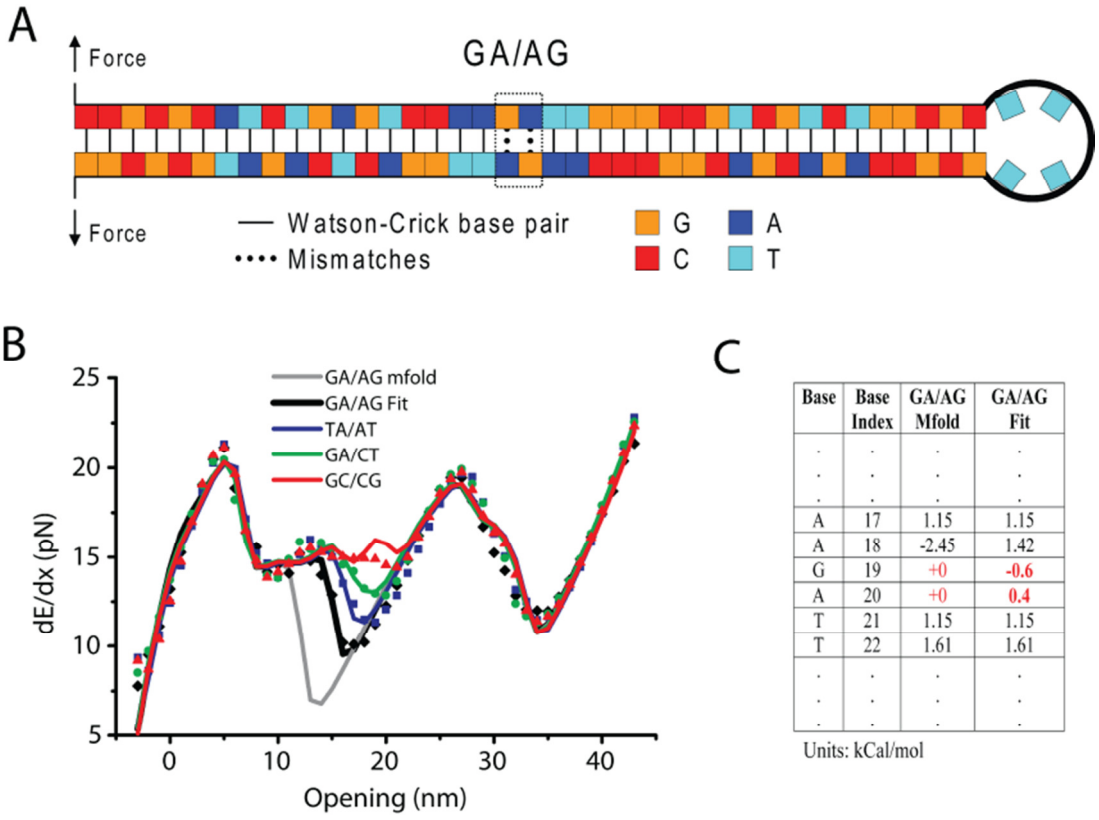

Base	Base Index	GA/AG Mfold	GA/AG Fit
.	.	.	.
.	.	.	.
.	.	.	.
A	17	1.15	1.15
A	18	-2.45	1.42
G	19	+0	-0.6
A	20	+0	0.4
T	21	1.15	1.15
T	22	1.61	1.61
.	.	.	.
.	.	.	.
.	.	.	.

Figure 1.8: (A) Hairpin sequence for the experiment. GA/AG was replaced by TA/AT, GA/CT, and GC/CG for control measurements. (B) dE/dx representation of the reconstructed energy landscape for tandem GA mismatch (black) and matched control sequences (TA/AT: blue. GA/CT: green. GC/CG: red). Symbol: measured value. Solid line: mfold prediction or our fit. (C) Free energy required to rip the hairpin at each base pair. Units: kCal/mol.

1.4.2 Dynamic Force Spectroscopy[1]

If the transition between states is irreversible, the above method for reconstructing the whole energy landscape is not valid; however, the properties of the energy barrier such as its distance and height can still be measured using dynamic force spectroscopy. DNA G-quadruplex is provided in this section as an example.

[1] This section is partially adapted from [18].

Guanine-rich sequences that can fold into highly-stable G-quadruplex conformations exist throughout the genome, often in pre-transcribed regions of genes [19–21]. Recent research provides evidence that G-quadruplex forms *in vivo* [22], has important regulatory functions [23], and could serve as a drug target [24]. G-quadruplex formation in the human telomeric repeat sequence is of particular interest because it can inhibit telomerase, overexpression of which is often found in cancer cells [25]. G-quadruplex occurs in different forms including RNA, single-stranded DNA, and double-stranded DNA accompanied by the corresponding C-rich i-motif structure [26].

In contrast to more typical stem-loop structures which can be disrupted progressively, G-quadruplex structures disrupt irreversibly when subject to a sufficiently large external force [27]. We used optical tweezers to study a single-stranded DNA G4-quadruplex from the insulin-linked polymorphism region (ILPR), located upstream of the insulin gene [28]. G4-quadruplex molecules were subject to a force which increased linearly in time until disruption was observed, or until the force reached an upper limit of ~50 pN. Dynamic force spectroscopy (DFS) was used to characterize the transition state energy barrier between the folded and unfolded conformation in terms of the distribution of disruption forces measured.

Several theoretical models have been put forward to predict the distribution of rupture forces that would be observed when a system with a single transition state barrier is subject to a force that increases linearly with time. A model proposed by Evans [29–31] has two free parameters, the barrier distance d and the zero-force unfolding rate k_o. More general models which include the zero-force transition state

barrier energy G [32,33] were subsequently refined by Dudko et al. [34] In the latter model the probability $p(F)$ that the structure ruptures at force F is given by

$$p(F) = \frac{k(F)}{r}\exp\left[\frac{k_o k_B T}{r d} - \frac{k(F) k_B T}{r d}\left(1 - \frac{\nu F d}{G}\right)^{1-\frac{1}{\nu}}\right]$$
$$k(F) = k_o\left(1 - \frac{\nu F d}{G}\right)^{\frac{1}{\nu}-1}\exp\left[\frac{G}{k_B T}\left(1 - \left[1 - \frac{\nu F d}{G}\right]^{\frac{1}{\nu}}\right)\right] \qquad (1.8)$$

where k_B is the Boltzmann constant, T is the temperature, r is the rate at which the force is increased, and ν is a dimensionless constant which parameterizes the shape of the energy barrier. Figure 1.9 represents the relationship between the assumed shape of the energy barrier and the value of the parameter ν. In the limit $\nu \rightarrow 1$, eq. (1.8) reduces to the Evans model [30]. The Dudko model has several advantages over the Evans model. It takes into account the variation of the transition state distance with applied force and it determines the transition state energy G.

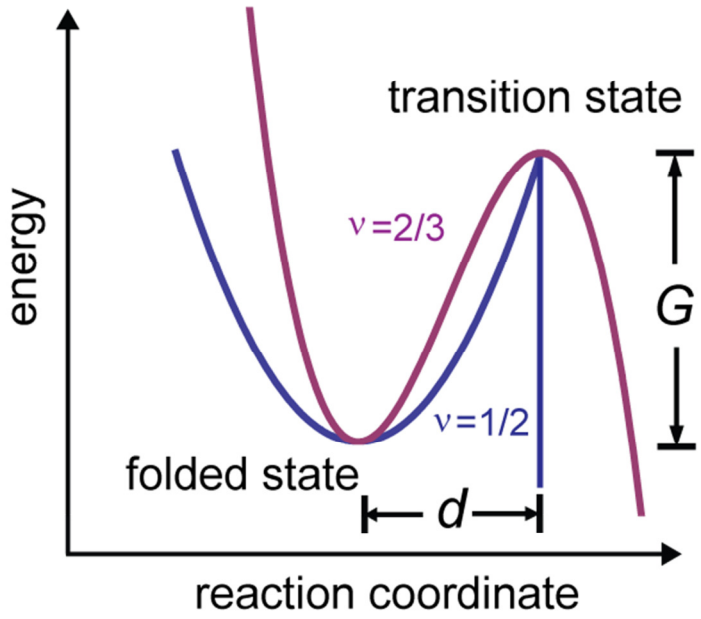

Figure 1.9: Definitions of parameters in Dudko model for $\nu = 2/3$ (purple) and $\nu = 1/2$ (blue). G and d represents the height and distance for transition energy barrier.

DNA G-quadruplex molecules between two handle DNA were attached to the surface through the digoxigenin label and attached to 0.82 μm diameter beads using the biotin label as shown in Figure 1.10. The experiment setup is similar to the ones used for energy landscape, except the force is now applied in both axial and lateral direction since larger force is required. Each sample was scanned repeatedly until the tether broke or the sample stopped showing any further disruptions. Between scans the sample was brought to a relaxed state at zero force for 5 seconds to allow the quadruplex time to refold. For each individual scan the initial force, the maximum accessible force, and the force of the observed disruption, if any, were recorded. Other experimental details are described in Appendix A: . We took data at three loading rates (2.1 pN/s, 7.0 pN/s, and 23.9 pN/s) for analysis using DFS. Two

populations of disruptions were resolved in the data, which have been identified in prior work as corresponding to parallel and antiparallel conformations [27].

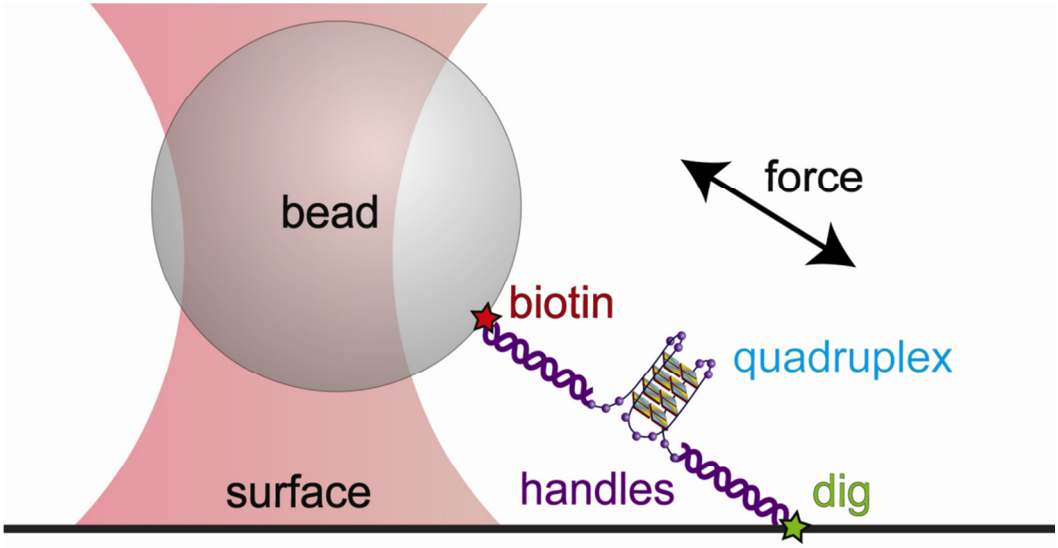

Figure 1.10: Experimental setup. The quadruplex is ligated between double-stranded DNA handles and attached to the surface and bead by digoxigenin and biotin labels respectively. Force is applied along the direction of the tether.

In order to obtain information on the properties of energy barrier, we fit our results to the Evans model ($v = 1$) and Dudko models ($v = 1/2$ and $v = 2/3$) using maximum likelihood (L_m). Models using these values of v can be solved analytically and are described in more detail by Dudko et al. [34] Since our disruptions exhibited the two peaks that have been identified as originating from parallel and antiparallel conformations, we based our analysis on a dual-component distribution. The likelihood L that an ensemble of measurements would be observed is defined as:

$$L(d_p, G_p, k_p, d_a, G_a, k_a, w) = \prod_i^N \left[w P_i(F_i \mid d_p, G_p, k_p; r_i, v) + (1-w) P_i(F_i \mid d_a, G_a, k_a; r_i, v) \right] \quad (1.9)$$

where the product is indexed over all scans and P_i is the theoretical probability density of observing a disruption event at force F_i and loading rate r_i for one of the two populations. The weight w indicates the fraction of the molecules in the parallel conformation (subscript p), while the fraction in the antiparallel conformation (subscript a) is $1–w$. A simplex search algorithm was used to find the values of d_p, G_p, k_p, d_a, G_a, k_a and w that produces the highest likelihood L (defined by Eq. (1.5)) for the measured distribution of F. (Indistinguishable results were obtained if the weight w was allowed to vary independently for each of the three loading rates.)

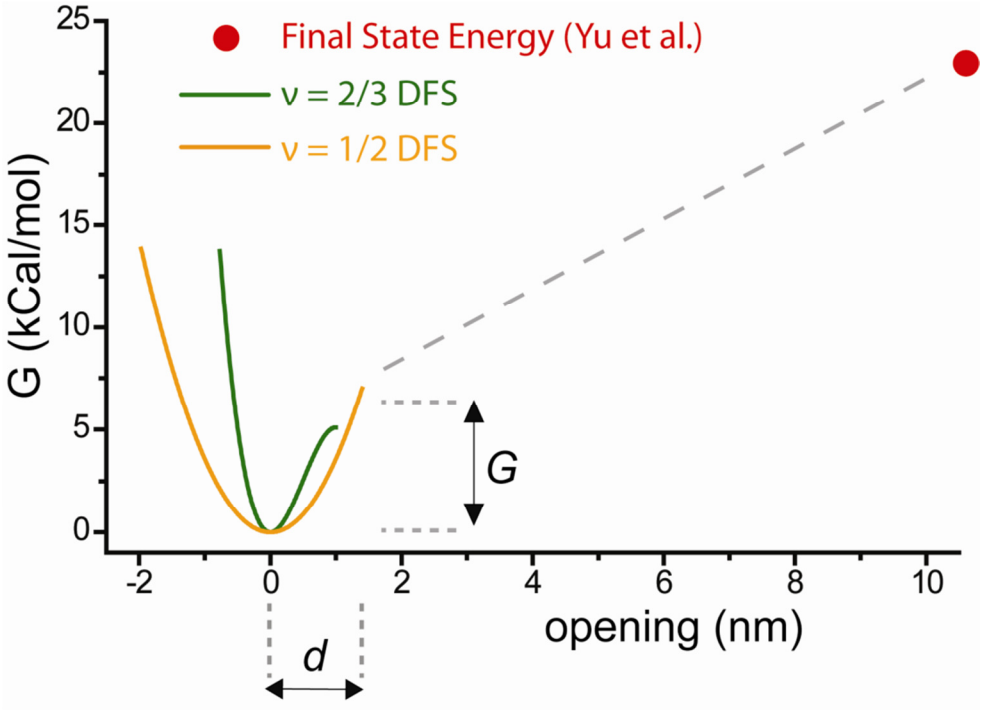

Figure 1.11: The Dudko models for $v = 2/3$ (green) and $v = 1/2$ (yellow) using parameters for d and G from fitting results in Table A.1: Summary of global maximum-likelihood fits for different values of v. $\ln(L_m)/L_0$ indicates the log of the maximum-likelihood score relative to the result for $v = 1$, normalized by $L_0 = \ln(N)/2$ where $N = 1014$ data points. Uncertainties were determined by bootstrapping. Weight (w) indicates the percentage allocated to the parallel conformation (subscript p) while the antiparallel conformation (subscript a) is allocated percentage (1–

***w*).Table A.1 for the antiparallel configuration. Dashed gray line indicates the undetermined region of the full energy landscape. DFS determines the primary barrier (yellow or green) but also constrains the landscape beyond the primary barrier to have a slope less than that leading to the barrier. Red shows the total free energy (23 kcal/mol) to unfold the antiparallel conformation, determined by Yu [27]).**

The best fit parameters for the three models as well as the corresponding likelihoods are summarized in Table A.1 and Figure 1.11, based on a total of $N = 1014$ disruptions. In Figure 1.12, histograms of disruptions at three different loading rates are compared to the global fit obtained for $v = 2/3$ (Table A.1). Blue and red represent the contribution from the parallel and antiparallel conformations respectively and green represents the sum of the two conformations.

The physical parameters obtained are relatively insensitive to the choice of v, allowing us to conclude that the G4-quadruplex energy barrier distance is approximately 10-16 Å, for both parallel and antiparallel conformations. The release of a nucleotide of single-stranded DNA will increase the tether length by approximately 5 Å, so this indicates that the transition state is reached after 2-3 bases have been pulled out of the structure. The transition state distance is a small fraction of the total amount of DNA released, and indicates that the transition state is much closer to the fully folded state than to the unfolded state.

A schematic model for disruption of the antiparallel conformation is shown in Figure 1.13. The model illustrates hypothetical symmetrical and nonsymmetrical disruption pathways for the antiparallel conformation, in which the first two base pairs are released from the same side or opposite sides of the structure, respectively.

(Analogous models can be formulated for the parallel case.) Formation of the quadruplex appears to be highly cooperative, in that a relatively small perturbation to the structure is required to reach the transition state and progress to complete dissociation.

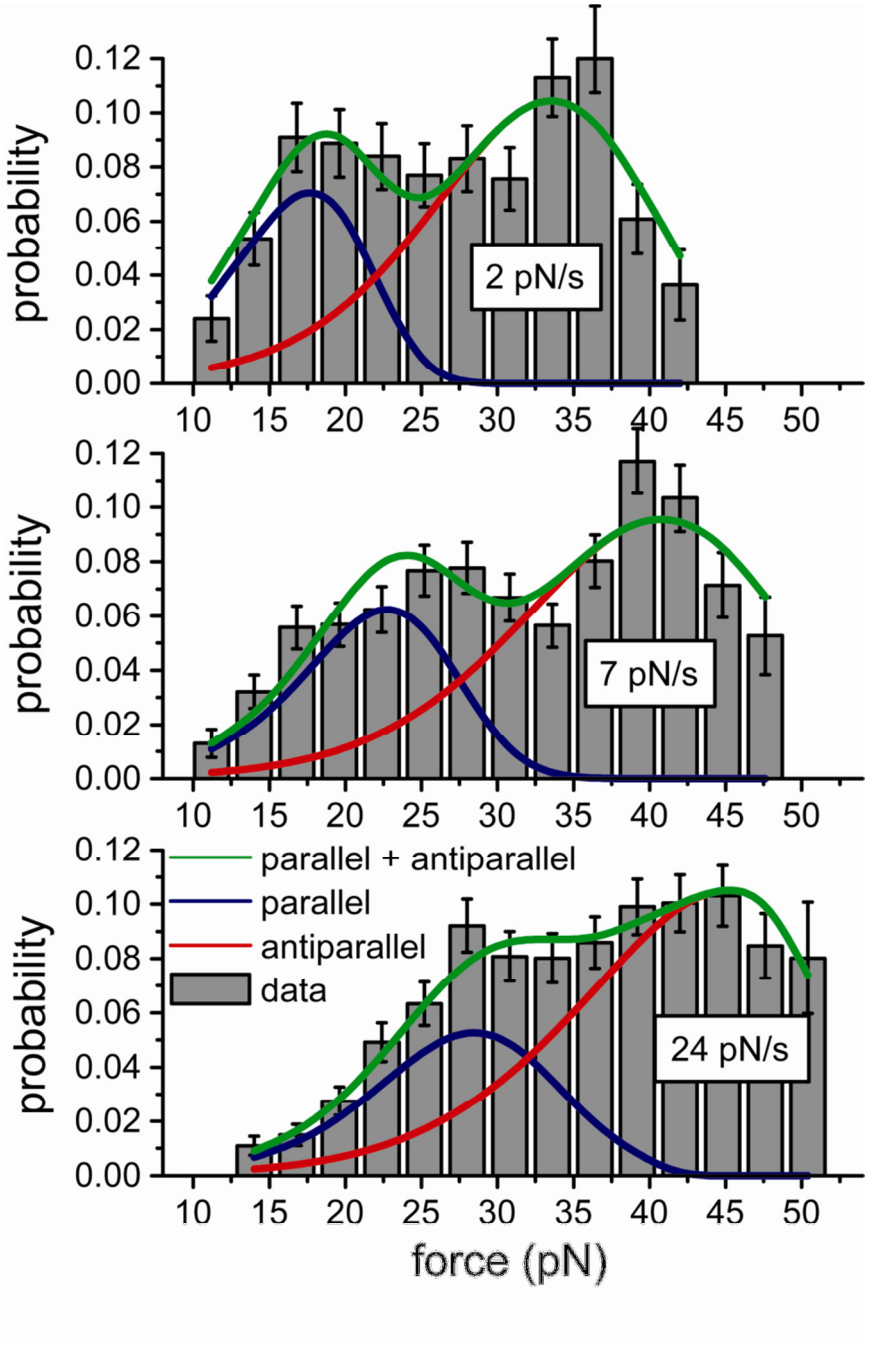

Figure 1.12: Global fit of G4-quadruplex data at three loading rates (2.1, 7.0, and 23.9 pN/s) for $\nu = 2/3$. Blue and red show the theoretical distribution for the parallel and antiparallel conformations respectively. Green represents the sum of the two conformations. The binned results are for representation only. The best fit was determined from maximum likelihood analysis.

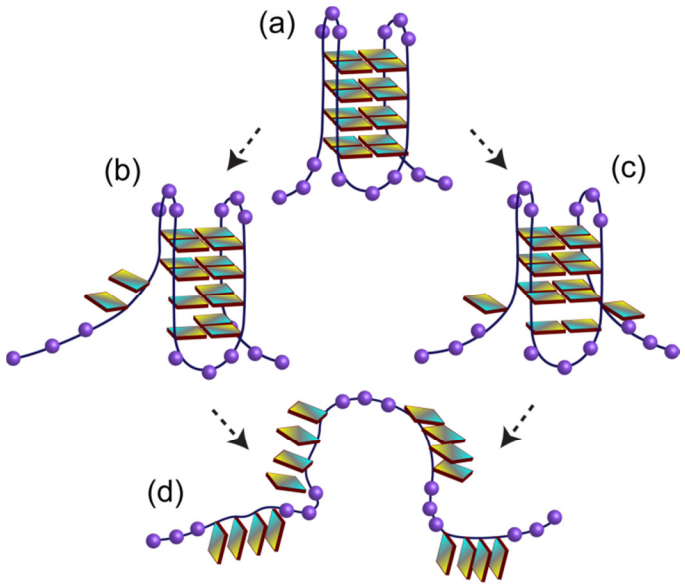

Figure 1.13: A model of G4-quadruplex disruption. (a) Original antiparallel conformation. Applied force causes two bases to be released from the G4-quadruplex, either antisymmetrically (b) or symmetrically (c). (d) Upon release of the 3rd base, the entire structure disrupts.

In conclusion, the energy barrier height and distance can also be measured using optical traps with DFS even the transition is irreversible. We have demonstrated this by measuring the disruption force and opening distance of a G4-quadruplex at three loading rates, resolving two force distributions which have previously been shown to originate in two distinct quadruplex conformations. The high mechanical stability previously demonstrated originates from the short steep barrier we measured for both forms of the quadruplex. These parameters have implications for regulatory

processes. The high-force resistance associated with the short barrier distance would make G-quadruplex difficult for a processive enzyme to disrupt. However, thermal fluctuations may assist an enzyme beyond the principal barrier where disruption can progress more easily.

1.4.3 Tracking Transcription Dynamics of single RNA Polymerase

Optical trapping is also used in another type of experiments where the dynamics of motor proteins can be tracked in real time, providing not only demonstrative result but also new insight into mechanism of many biological processes. The molecular motors that have been studied in this manner include DNA polymerase, RNA polymerase, ribosome, kinesin, etc [35–39].

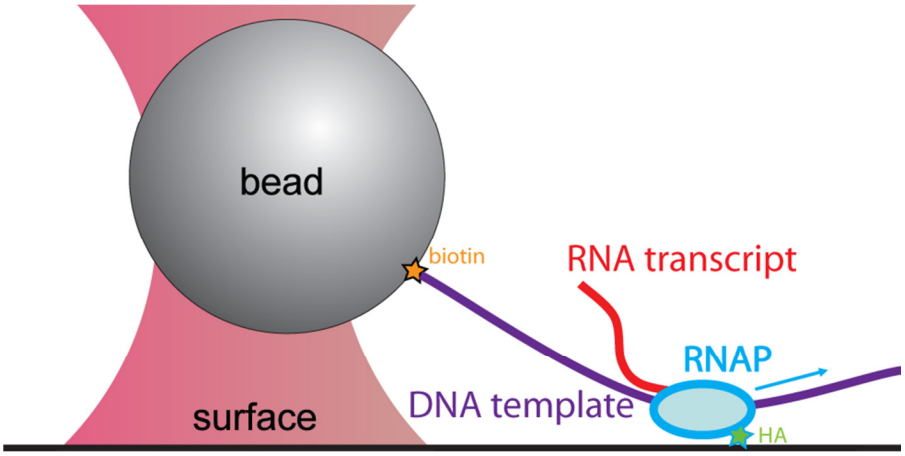

Figure 1.14: Experimental setup for studying transcription dynamics of RNA polymerases in assisting mode. Force on the bead can be controlled by adjusting laser power. When transcription starts, the length between RNAP and the bead increases and is recorded in real time.

We apply optical trapping to study transcription at the single-molecule level. As shown in Figure 1.14, a transcribing RNA polymerase attached to the surface changes the DNA template length that can be recorded in real time. By analyzing time traces of RNAP position on template DNA, the dynamics of transcription can be obtained. Assisting or resisting force can be added depending on the template direction. Figure 1.15 shows an example traces. The speed distribution of RNA polymerase is bimodal, representing pausing and transcribing states. Less frequent events during transcription such as pausing and backtracking of the RNA polymerase are also observed. Upon collecting many traces, the pause density or pause-velocity relation can be studied [40–42].

An application of this method is to investigate the role of transcription factors in gene regulation [43]. A more complicated assay can be used to directly observe polymerase transcribing through nucleosomes [44–46]. Along with optical torque wrench, both positional and angular information can be collected simultaneously. These experiments will potentially provide detailed insight into the central dogma of molecular biology.

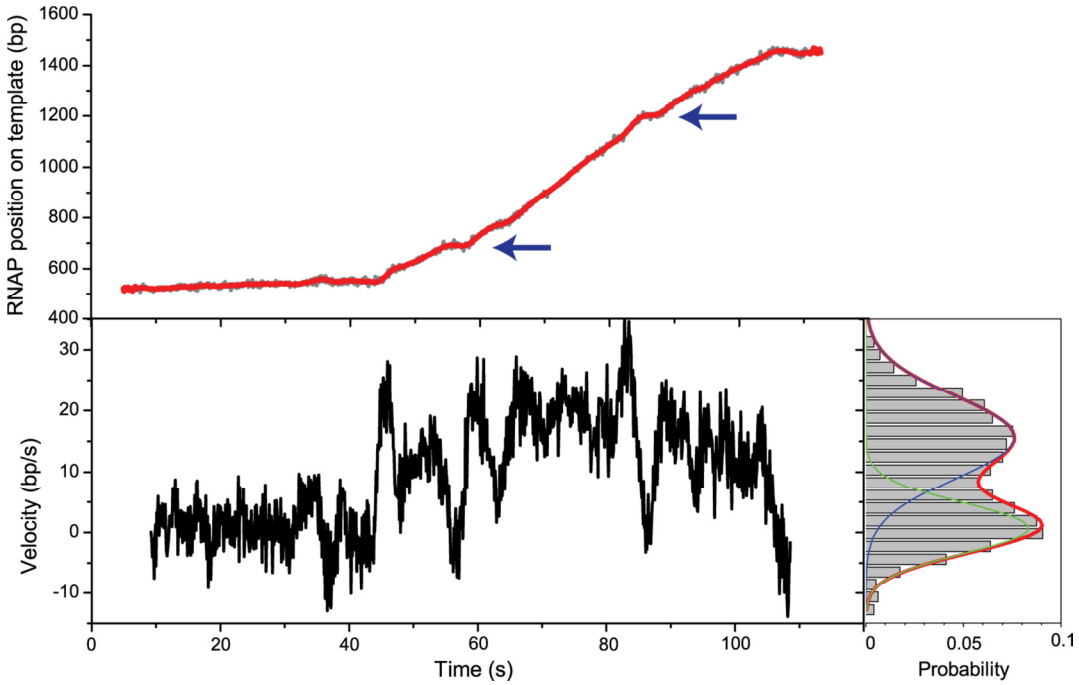

Figure 1.15: Representative trace of RNA polymerase (RNAP) transcribing template DNA under 3 pN assisting load. (a) RNAP position on template as a function of time. Arrows show where RNAP paused shortly and restarted. (b) Instantaneous velocity of RNAP. (c) Velocity distribution fits well to the sum of two Gaussians indicating two states with velocity 15.6 ± 0.4 bp/s (transcribing) and 0.7 ± 0.3 bp/s (pausing).

1.5 Improving Optical Traps

Surface drift is a source of error in the surface-based optical trap. For experiments with a longer time scale of minutes such as transcription, it would lead to difficulties. Although a dual trap setup is free of contact with the surface, precluding drift issue and leading to higher stability, a surface-based assay is simple to apply and necessary for angular manipulation introduced in the next chapter. While maintaining the original optical trap setup, we develop an independent measurement to track the

surface height by sending in another weak laser beam and detect the reflection due to surface height change.

The principle is shown in Figure 1.16. A separate weak laser beam is scanned by acousto-optical modulator (AOD) from red to green. The reflective beam goes back to the same spot if the cover glass is not moved. If we place a position sensitive detector in the conjugate plane of AOD, the small drift of cover glass will translate to a scanning dot on the detector. Since the input laser is modulated by AOD, we can measure the PSD signal for the certain frequency using lock-in amplifier.

Figure 1.17 shows an example that we move the cover glass by a piezo stage. The detected height tracking signal can follow the stage command. Our results show that it can be sensitive to one nanometer of cover glass drift. Therefore, the calibrated signal can be used for feedback control on the surface height when a real single-molecule experiments is performing, increasing the spatial resolution.

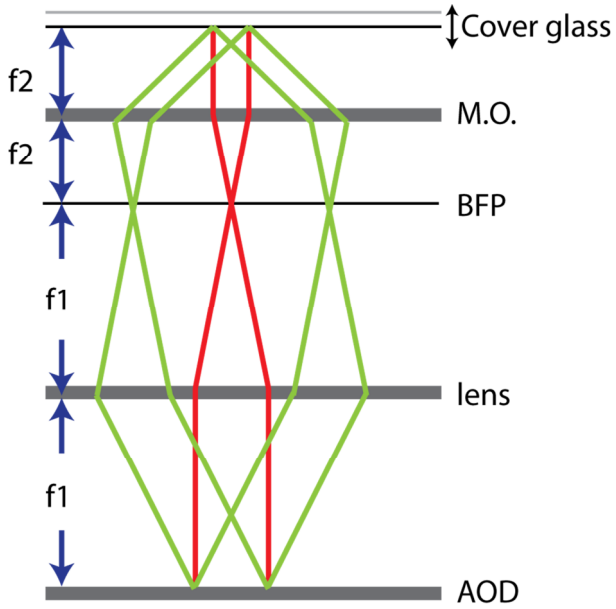

Figure 1.16: Setup for height tracking beam. The scanning laser enters from below and reflected by the cover glass and goes back to the same spot if the cover glass is not moved. AOD: acousto-optical deflector. BFP: back focal plan. M.O.: microscope objective.

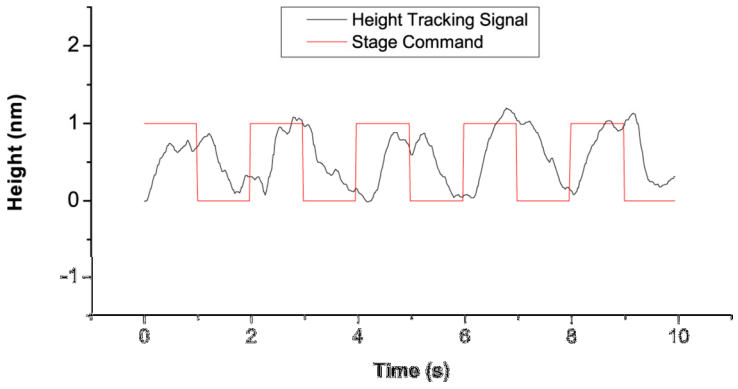

Figure 1.17: A piezo stage moves the coverslip in axial direction for a step of one nanometer is followed by the height tracking signal.

Chapter 2: Optical Torque Wrench

2.1 Introduction

Optical tweezers and its applications have been introduced in chapter 1. While most experiments using optical tweezers characterize force and displacement, torque and angular motion play significant roles in biological phenomena such as DNA replication and transcription [47], ATP synthesis [48] or bacteria propulsion [49,50]. However, there have been relatively few reports on torque and angular measurements of bio-molecule due to limited methods to directly manipulate and detect such quantity. In this thesis, effort has been put to develop such technique based on optical traps.

In this chapter, we first present the principle for angular trapping. Two different particles used for angular trapping in this thesis are squashed microspheres and birefringent quartz cylinders. Methods for fabricating large quantities of birefringent cylinders rapidly and at low cost using nanosphere lithography (NSL) [51,52] is developed and detailed here. The design consideration is described and compared with other methods. Nanocylinders of diameter ~500nm and height ~800nm are shown to provide stable angular trapping in optical torque wrench (OTW) for single-molecule experiments. Finally, force and torque generated using the cylinders are calibrated, and linear and angular manipulations of twist-stretched DNA are demonstrated and discussed.

2.2 Principle

The optical torque wrench [53,54] has been developed for angular manipulation and precise detection of torque via an optically anisotropic particle trapped in a laser beam. Figure 2.1(a) shows a birefringent particle whose ordinary axis (χ_o) and extraordinary axis (χ_e) misaligned to the external electric field. As a consequence, a restoring torque (τ) from the cross product of induced polarization (P) and external electric field (E) tends to align the extraordinary axis with the external electric field. The resulting torque can be quantified by measuring the spin angular momentum transfer of the photon, i.e. imbalance of left- and right-circular components of the transmitted beam as shown in Figure 2.1(b).

Figure 2.2 shows a typical OTW setup for single-molecule experiments. Similar to an optical trap setup using microsphere, the target bio-molecule is now attached with one end to the glass slide and the other end to a birefringent particle (not necessarily a cylinder) trapped by a tightly focused Gaussian beam. Controlling the position of surface and state of the input laser beam allows us to simultaneously stretch and rotate the molecule. Note the multiple attachments make the torsion added to the molecule possible. Force and torque response is detected by monitoring the position and polarization state of the transmitted trap beam.

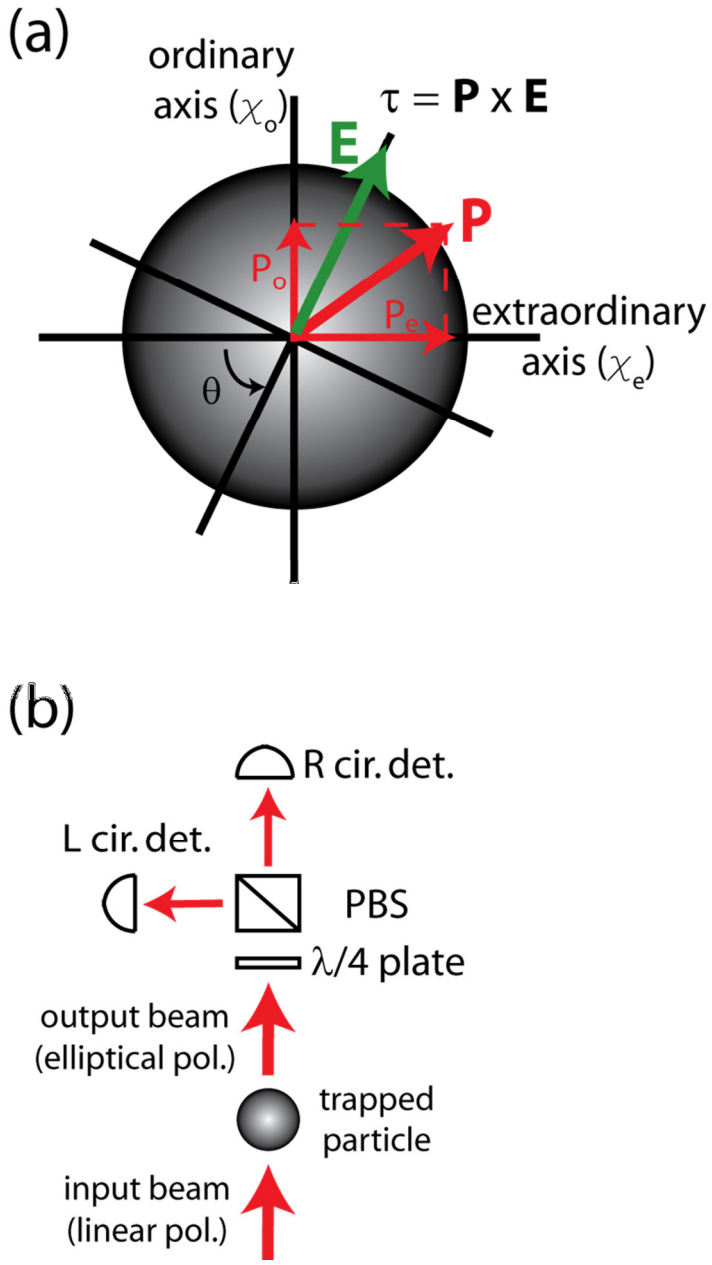

Figure 2.1: (a) Schematic diagram of an anisotropic particle whose extraordinary axis misaligned to the external electric field (*E*). Torque is generated when induced polarization (*P*) is not aligned to the electric field (*E*). (b) Schematic diagram of the torque detection in OTW. The torque signal is measured by detecting the imbalance of left- and right-circular component of the scattered beam. PBS: polarizing beam splitter.

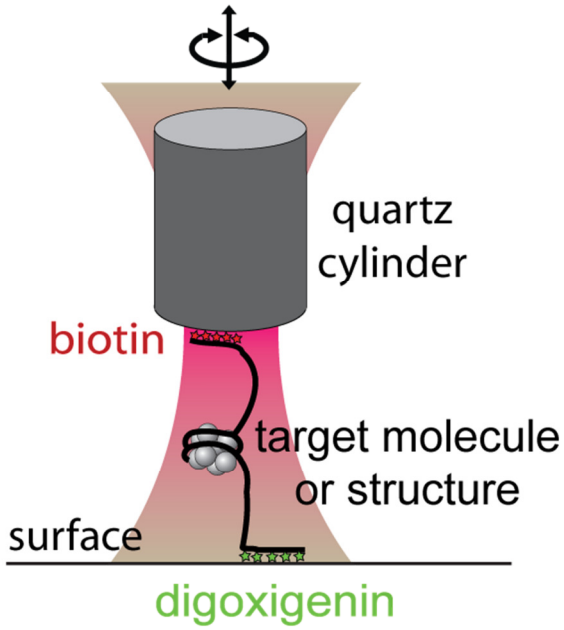

Figure 2.2: Schematic of OTW setup using fabricated quartz cylinders for single molecule experiments. The target bio-molecule is rotationally constrained. tethered to the cylinder which is linearly and angularly manipulated by controlling both laser and surface.

2.3 Sources of Optical Anisotropy

Efforts have been emphasized to design and fabricate an optimal particle in OTW [55–57]. The requirement of optical anisotropy can be obtained from shape or material.

2.3.1 Squashed Microsphere

In the case of form birefringence, anisotropic shape and the resulting anisotropy of polarizability make angular trapping possible. For instances, oblate particles were used in previous works [58]. We start with this particle in our OTW setup.

The oblate particles are obtained by mechanically compressing polystyrene microspheres [58,59]. Microspheres of 970 nm diameter were suspended in water (<2% by volume) and flattened between two slides mounted in a vise with two machined aluminium blocks. The vise is padded with rubber to maintain uniform pressure. The compression is achieved by tightening four bolts holding the vise and maintaining the pressure for 5 min at room temperature. The deformed particles are collected by washing the slide and scrapping with a blade. Microcentrifuging is used to concentrate the product. A fraction of pressure-treated particles have aspect ratio ~3 which can be easily distinguished in a light microscope. We note that the yield and uniformity of good squashed particles is related to the suspending concentration which needs to be optimized because higher starting concentration tends to lower the yield but smaller starting concentration requires many cycles of compression to obtain enough particles for experiments.

These squashed particles can be stably trapped in optical traps. Furthermore, using the optical torque wrench setup, it can be rotated by controlling the direction of polarization of input laser beam, as shown in Figure 2.3. Furthermore, a rotationally-constrained DNA is attached one end to biotin-coated oblate particle and the other end to the surface, allowing us to apply rotation along its axis. The unwinding of DNA after turning off the laser acts as a rotational spring and can be observed by the reverse rotation of the particle.

In chapter three, the oblate particles are used for studying mechanical stability of mononucleosome under tension and torsion.

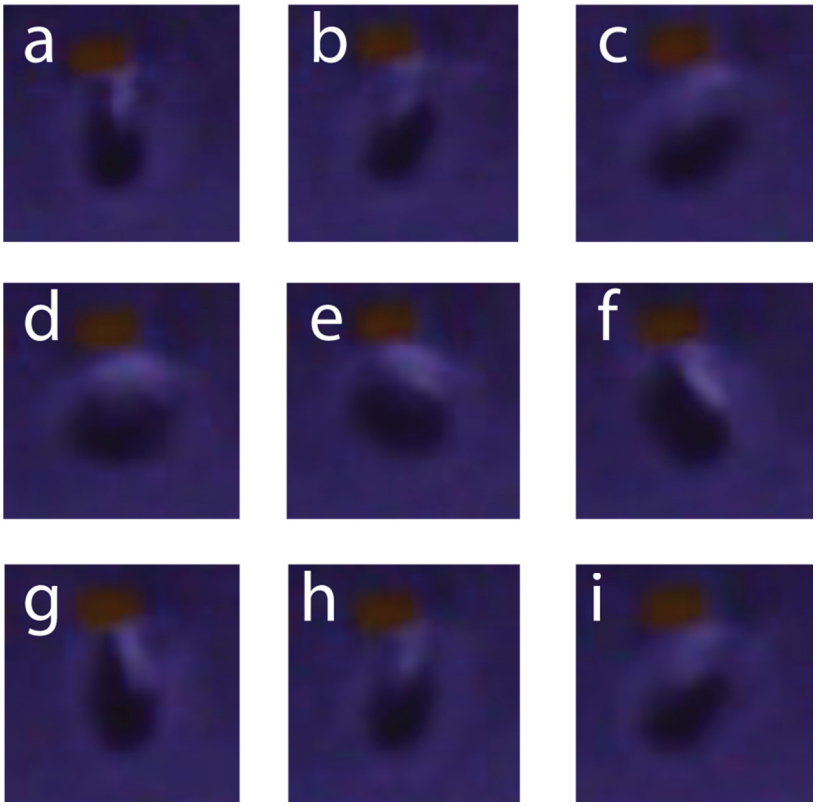

Figure 2.3: A sequence of bright field images (a-g) for an oblate particle being rotated in the OTW. The particle is squashed from 970 nm polystyrene microsphere. Time between frames is 0.1 s. White rectangle is a fixed object for visual reference.

2.3.2 Nanofabricated Quartz Cylinders[2]

Although it is possible to perform single-molecule experiments using squashed microsphere, there are several difficulties. First, the yield for compression procedure is low. Second, the uniform coating of biotin makes the searching for ideal geometry time-consuming. The DNA molecule has to be tethered to the equatorial position for a

[2] Collaboration with Edward T. Yu lab, The University of Texas at Austin.

successful experiment, which is statistically a rarer event. Moreover, the non-uniformity causes the difficulties to obtain converging results.

Birefringent quartz cylinders are devised and fabricated recently for use in OTW and have several advantages. First, the fabrication process makes it easy to produce with large quantity and high uniformity. Second, the elongated shape makes the symmetric axis of the cylinder aligning with the propagation direction of the incident light, leaving the only rotational degree of freedom to be controlled by the external field. Finally, for the use in single-molecule experiments, the cylinder can be selectively functionalized only on the top surface, increasing the efficiency in searching appropriate geometry for measurement.

Previous methods for fabricating such cylinders are achieved by optical [59,60] or electron beam lithography [61]. However, these fabrication methods are either restricted by minimum feature due to diffraction limit or extremely time-consuming, and generally very expensive. We develop a fabrication process using nanosphere lithography (NSL). NSL has been previous developed and applied in anti-reflection coating, sensing, and photovoltaics [52]. We adapt the NSL technique and fabricate quartz nanocylinders with tunable sizes.

The fabrication process and consideration for optimizing experimental parameters are detailed here.

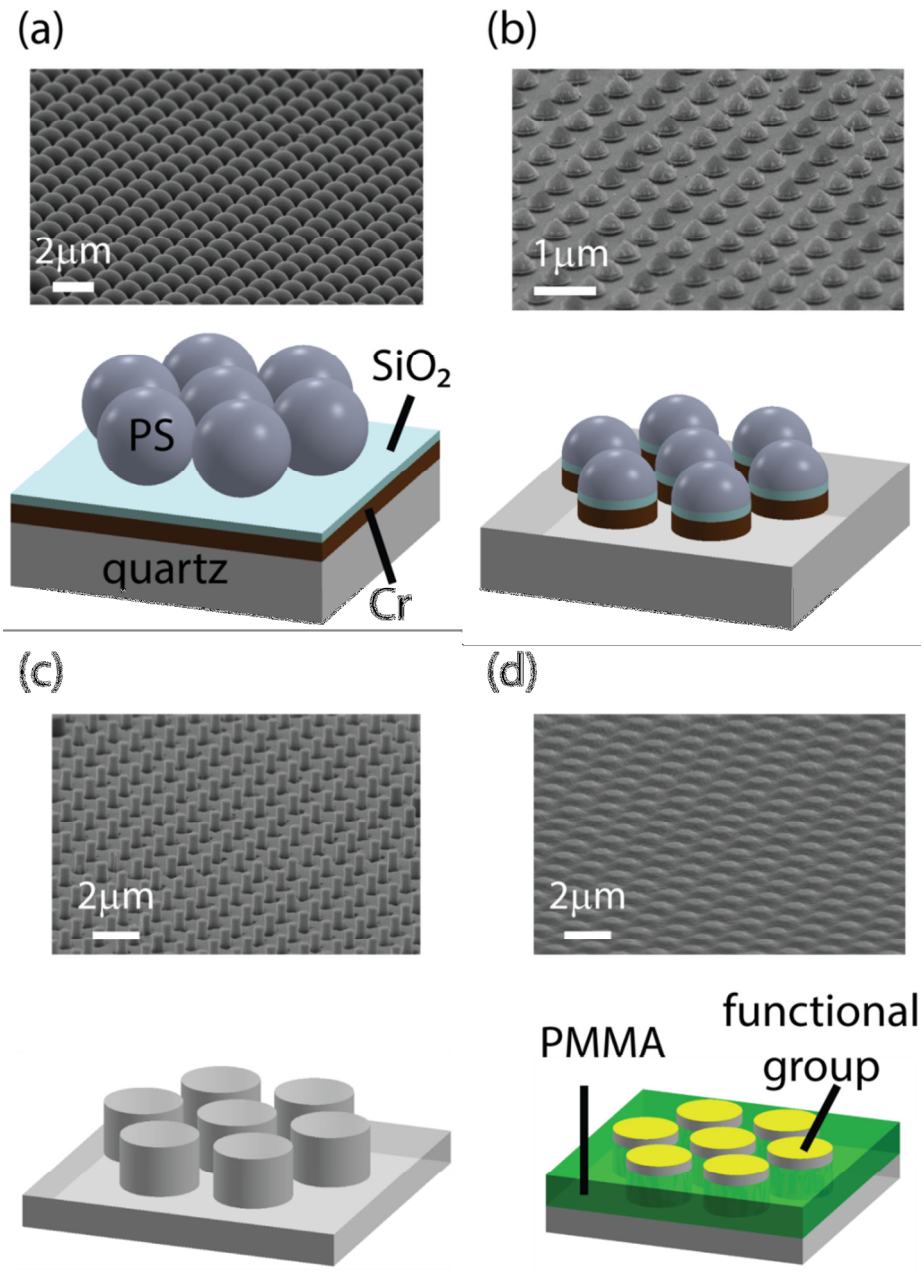

Figure 2.4: Schematic diagram of the fabrication process flow and scanning electron micrograph at each step: (a) A single crystal quartz substrate is covered with 10nm Cr/100nm SiO_2, followed by NSL using 2μm diameter PS nanospheres. (b) A series of dry etching process is used to reduce the sphere size and transfer the hexagonal lattice pattern to the underlying Cr layer. (c) Nanocylinders form by single crystal quartz by drying etching using Cr mask which is later removed by wet etch process. (d) Nanocylinder buried in PMMA with only the top surface exposed to amino-group functionlization.

Figure 2.4 shows the key fabrication process for the birefringent nanocylinders. The single crystal quartz substrate (X-cut, University Wafer) is first cleaned with piranha solution (mixture of 30% H_2O_2 and 96% H_2SO_4 with a volume ratio of 1:2, from Sigma Aldrich) for 30 minutes. The single crystal quartz (X-cut) substrate is deposited by 90nm Cr/10nm SiO_2 by e-beam evaporation. A self-assembly monolayer of 2μm diameter polystyrene (PS) nanospheres is then deposited on the SiO_2 surface using Langmuir-Blodgett method [51] as shown in Figure 2.4(a). A clean Petri dish filled with deionized water, and a clean glass conduit placed ~60^o on the side are prepared. The diluted PS solution (mixture of Ethanol with volume ratio of 1:1, from Sigma Aldrich) is slowly injected onto the conduit into the water-air interface, and the resulting PS monolayer can be observed as a colored layer due to diffraction. After aggregation of sufficiently large area, the PS monolayer can be transferred to the Cr/SiO_2 coated quartz substrate. For our implementation of this process, defect-free hexagonally close packed regions of nanospheres typically extend over distances of ~100μm, separated by cracks between boundaries and a few vacancies.

Reactive ion etching (RIE) is used to etch the PS spheres to reduce the diameter to 1.5-1μm depending on etch time. As a guide, the diameter of the nanospheres is reduced by RIE with 200sccm of O_2 and radio frequency (RF) power of 200W for 5-7 mins, resulting in nanospheres of 1.5μm to 1μm. These nanospheres then serve as an etch mask to transfer the hexagonal pattern to the underlying Cr, which acts as a hard mask with diameter ~500nm during the subsequent quartz

etching process to achieve the desired high aspect ratio structure as shown in Figure 2.4(b).

The quartz substrate with Cr hard mask on top underwent RIE with 20sccm of CHF_3 and RF power of 100W for 60 minutes to provide ~800nm height as shown in Figure 2.4(c). The Cr mask and residual polymer resulted during dry etch is removed by a standard wet etch process (Transene chromium etchant 1020). The diameter of the nanocylinder is typically ranged from 50nm to 1μm depending on the size of the sphere and total etching time and the height of nanocylinder is ranged from 1μm to 2μm, depending on the thickness of Cr mask. We note that the resulting torque in OTW is proportional to the size of the nanocylinder since the signal is measured by the total angular momentum transfer of the nanocylinder. The aspect ratio of the nanocylinder should be also large enough to assist the alignment of the long axis of the nanocylinder with the laser beam. With these considerations, the final size of fabricated birefringent nanocylinders with diameter ~500nm and height ~800nm are proven to be suitable for single-molecule experiment in OTW.

In Figure 2.4(d), the cleansed substrate is then spin coated with PMMA, and etched away the excess PMMA so that only the top surfaces of the nanocylinders are exposed. For application in single-molecule experiments, we selectively functionalize only the top surface of the nanocylinder with amino group which is necessary for further avadin coating. The above wafer is incubated in 1% Vectabond reagent (Vector Laboratories, Inc.) for 5 minutes and transferred to acetone for 30 minutes to remove PMMA. The wafer is air-dried and cylinders are collected using microtome

blade (C.L. Sturkey, Inc.) Last, Avadin (Vector Laboratories, Inc.) are coupled to amino-functionalized cylinder using Glutaraldehyde kit (Polysciences, Inc.)

Individual nanocylinders are collected by manually scraping with microtome blade as shown in Figure 2.5**.** The size distribution mainly due to the limit of RIE machine is measured by SEM and shown in Figure 2.6. We note that the distance between each nanocylinder and the aspect ratio is crucial to avoid incomplete removal of the nanocylinders and undesired quartz residues. The 4 inch quartz wafer is typically used and processed, providing ~10^8 nanocylinders which is sufficient for calibration and measurement of single-molecule experiment. Compared with conventional lithographies, NSL is a rapid, low-cost, large-area nanoscale patterning technique with a wide range of size choices.

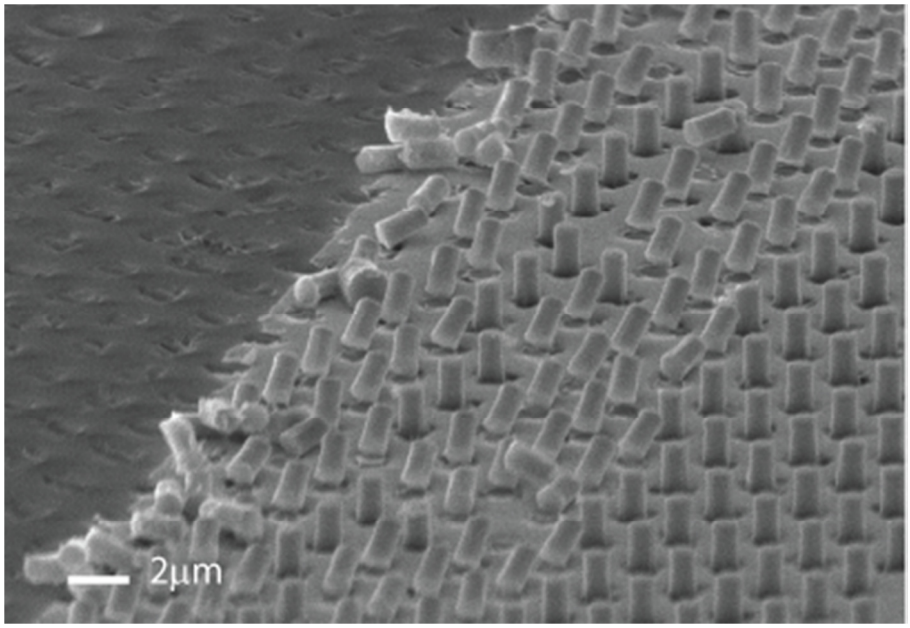

Figure 2.5: SEM image shows single quartz cylinders can be mechanical removed and collected for single-molecule experiments.

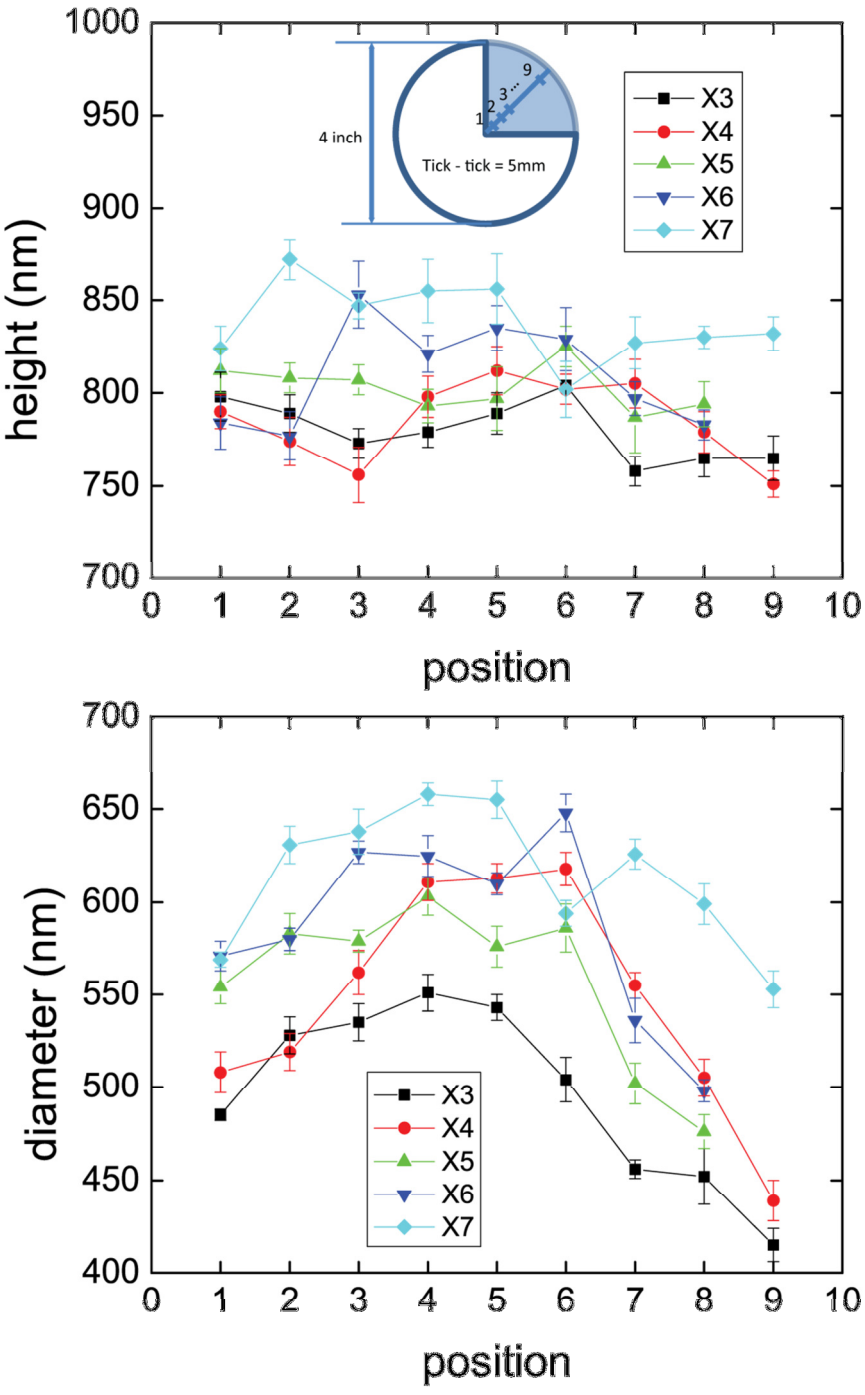

Figure 2.6: Distribution of height and diameter for cylinders on a wafer measured by SEM image. X3-X7 corresponds to different batches using various parameters.

2.4 Mechanical Design

The optical torque wrench setup is modified based on a standard optical tweezers described in chapter 1. Figure 2.7 shows the schematic of setup. The major difference is the incorporation of a half wave plate mounted on a motorized rotator (NSR1, Newport Corporation) for controlling linearly-polarized laser beam. A more sophisticated setup can be used with electro-optical modulator (EOM) for faster control of polarization state of input beam [59]. For the experiment considered in this thesis, a rotating half wave plate satisfied our purpose and is simpler to apply. The torque is measured by the angular momentum transfer between the nanocylinder and the photon detected via imbalance of left- and right-circular component of the outgoing beam.

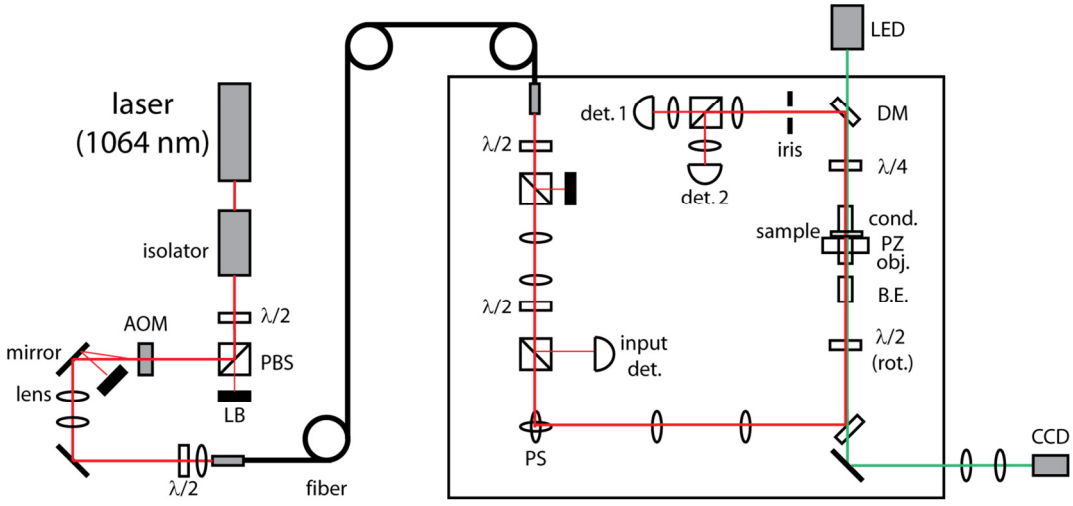

Figure 2.7: Schematic diagram of optical torque wrench setup. LB: laser block. λ/2: half-wave plate. PBS: polarizing beam splitter. DM: dichroic mirror. cond: condenser. PZ: piezo stage. B.E.: beam expander. PSD: position sensitive detector. PS: periscope.

2.5 Calibration

Accurate calibration of force and torque is required to perform precise quantitative measurements for a trapped nanocylinder in OTW. For the cylinders of size discussed here, the calibration of force and position follows the standard protocol for polystyrene (PS) particle of similar dimensions in optical tweezers as described in chapter 1.

Analogous to force calibration introduced in chapter 1, the calibration of torque and rotation can be achieved by measuring the power spectrum of torque signal (intensity difference in two detectors) for a trapped nanocylinder [53,59,62]. The power spectra of torque signal can be fitted by a Lorentzian line shape due to Brownian fluctuations in rotational motion [7]. This Lorentzian characteristic is therefore modelled as

$$S_\theta(f) = \frac{A_\theta^2}{f^2 + {f_{0,\theta}}^2} \qquad (2.1)$$

with corner frequency

$$f_{0,\theta} = \frac{\alpha_\theta}{2\pi\gamma_\theta} \qquad (2.2)$$

and amplitude

$$A_\theta^2 = \frac{k_B T}{\pi^2 \alpha_\theta} \qquad (2.3)$$

where α_θ is the angular stiffness of the trap, γ_θ is rotational drag coefficient, k_B is the Boltzmann constant, and T is temperature in degrees Kelvin.

As shown in Figure 2.8(a) we observe that the measured power spectrum for a birefringent nanocylinder is in good agreement with the fitted Lorentzian line (solid line), showing the birefringent nanocylinder is angularly trapped; whereas the PS

nanosphere (diameter 820 nm) is not trapped due to the lack of birefringence. The angular sensitivity is measured by rotating polarization on a cylinder fixed to the surface. Figure 2.8(b) shows that the torque signal modulates sinusoidally, where θ rotating at 1.8 rad/s is the angle between the direction of electric field and the extraordinary axis of the nanocylinder as shown in Figure 2.1(a) and V_0 is the maximum voltage obtained at θ=45°.

Therefore, any measured torque signal V_θ can be converted to physical unit by

$$\tau = \frac{V_\theta \alpha_\theta}{2V_0} \qquad (2.4)$$

Using the fitted parameter $f_{0,\theta} = 204$ Hz and $A_\theta^2 = 9.8 \times 10^{-5}\text{V}^2\text{Hz}$ from example data as well as $V_0 = 0.11$ V in Figure 2.8, we obtain γ_θ=2.1 pN.nm.s, $\alpha_\theta = 2.6 \times 10^3$ pN.nm/rad, and torque signal sensitivity 1.2×10^5 pN.nm/V. We note the experimentally determined rotational drag coefficient here is consistent with other experimental [62] and theoretical works [63] for nanocylinders with similar dimensions. The maximum torque which can be generated is ~1300 pN.nm, given the nominal laser power ~300 mW measured before rotational half-wave plate.

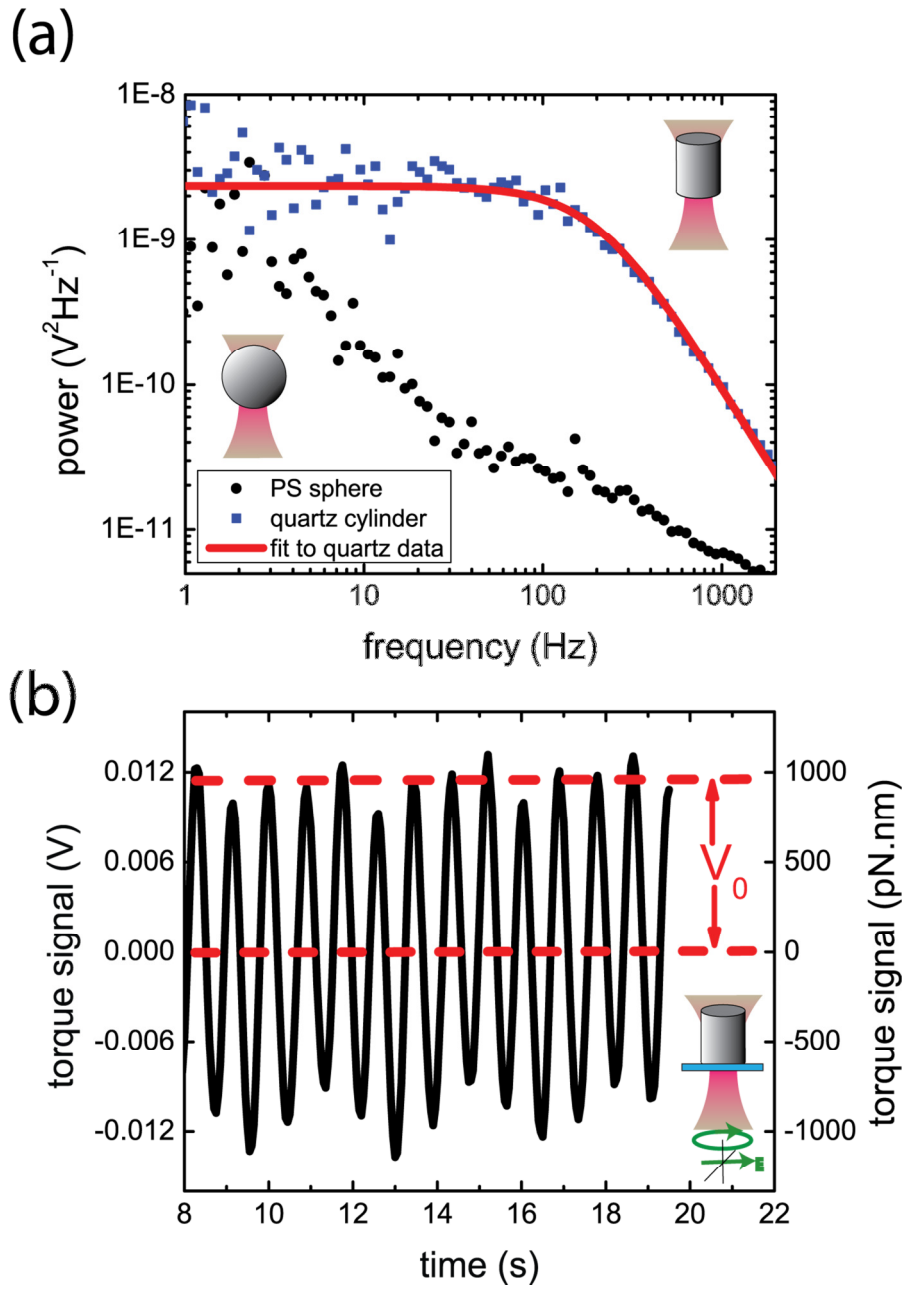

Figure 2.8 (a) Measured power spectra of torque signal for birefringent nanocylinders and PS spheres with radius of 410nm. The solid line indicates the Lorentzian fit for birefringent nanocylinders. (b) Torque signal of a fixed birefringent nanocylinder scanned by a rotating polarization vector.

2.6 Application to Twist and Stretch DNA

We further demonstrate the application of the birefringent nanocylinder in single-molecule experiment by measuring a twisted and stretched DNA undergoing structural transition. The twisted state of DNA is regulated *in vivo* by topoisomerases and influences the accessibility of DNA to many motor proteins. Therefore the mechanical properties of DNA under tension and torsion have profound implication in many biological contexts.

Using feedback to the surface position we apply constant force on a torsionally constrained double-stranded DNA (dsDNA) as the cylinder is rotated and record the extension of the dsDNA as a function of rotation turns added. The rotationally-constrained DNA was ligated from three pieces of DNA made separately by polymerase chain reaction (PCR). Two short pieces incorporate multiple digoxigenin (322 base pairs) and biotin (336 base pairs) labelled nucleotides, which allows for torsionally constrained binding to the sample chamber surface and cylinder respectively.

Figure 2.9 shows the measured and theoretically modelled extension of dsDNA recorded as a function of rotations under different stretching forces. Positive rotation is defined as the direction to overwind dsDNA. With positive torsion, the extension curves remain constant at low total turns (<3). Over this region, the extension of dsDNA starts to drop abruptly and monotonically as total turns are added, indicating the dsDNA buckles to form a plectoneme. The critical number of turns for this sharp transition increases with the applied force due to the increased rigidity of dsDNA under tension. Upon negative rotation, the extension responses with higher force (2.5

and 3.6pN) remain almost constant because dsDNA prefers to unwind rather than buckle, therefore no plectoneme is formed. For lower force (1pN), the dsDNA unwinds and buckles simultaneously when the total applied turn increases so that the extension curve drops without a sharp transition. Finally, for even lower force (0.3pN), the symmetric extension response is expected by phase transition model [64,65]. The force is small enough such that unwinding of helix structure is unfavourable and only the stretched and plectonemic states are allowed. These characteristics we observed are consistent with measurement performed using magnetic tweezers [66,67] and OTW [68–71].

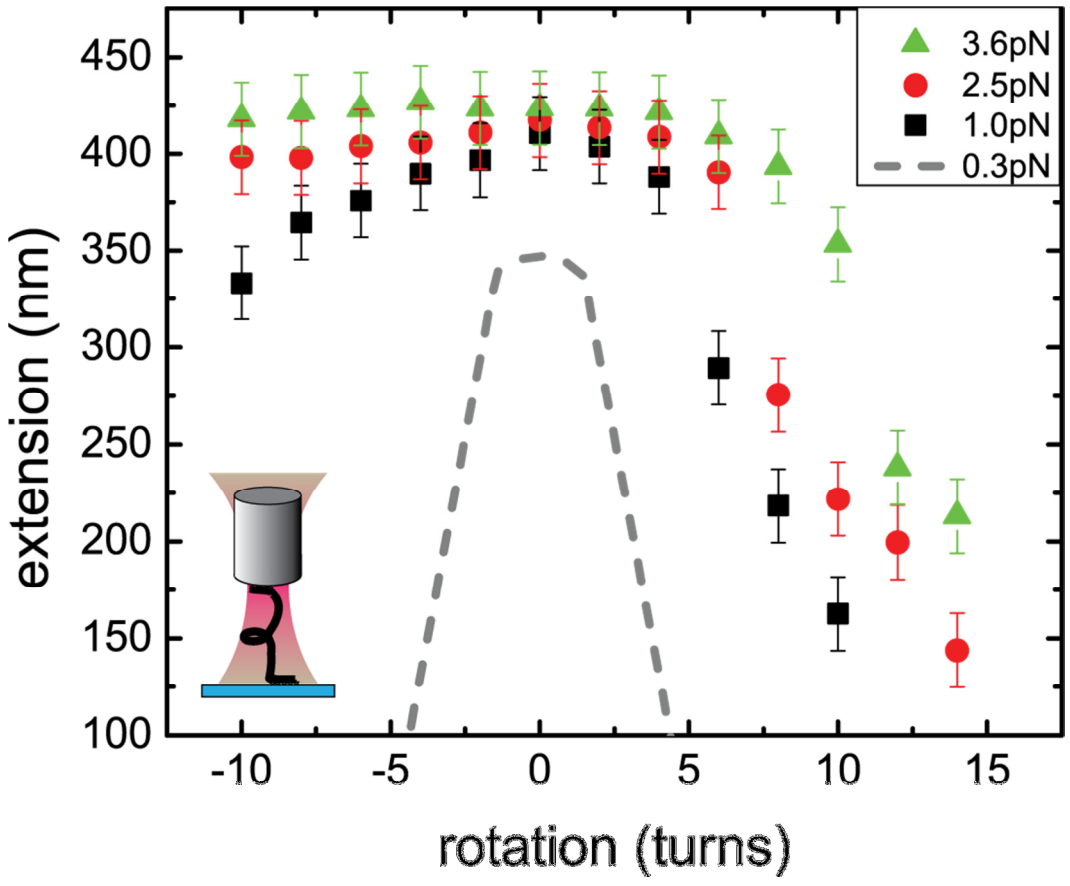

Figure 2.9: Measured rotation-extension curve for a double-stranded DNA at different fixed forces. Gray dashed line indicate model prediction for low force limit.

2.7 Summary

In this chapter, we described the quest for angular manipulation and torque measurements in single-molecule experiments. In developing optical torque wrench for this purpose, we use oblate polystyrene particles as well as developing novel technique to fabricate quartz cylinders. Large quantities of birefringent nanocylinders are fabricated by low-cost, rapid-patterning nanosphere lithography, and the use in single-molecule manipulation of dsDNA with optical torque wrench is demonstrated. Nanosphere lithography is superior to conventional lithographies with wide range of sizes, uniformity and quantities compared with previous approaches. The requirements in optical trapping and fabrication details of these birefringent nanocylinders are also discussed. The calibration of force and torque in optical torque wrench, together with a measured extension curve of double-stranded DNA is demonstrated experimentally to confirm the compatibility of our birefrigent nanocylinders in optical torque wrench.

Chapter 3: Mechanical Stability of Single Nucleosome

In this chapter, we apply the optical torque wrench to probe the mechanical stability of nucleosome under both tension and torsion. Prior studies have exerted linear tension to stretch single or multiple nucleosomes, providing information on the nature of the free-energy barrier for a particular disruption pathway. However, not only force but also torque is generated by helicases, polymerases, and other motor proteins to progress through the nucleosome. Therefore, it is important to examine the influence of torsion on nucleosome stability. Here, using optical torque wrench, we disrupt mononucleosomes under constant twist. Positive supercoiling is found to lower the mean disruption force while negative twist does not change the disruption behavior significantly. We further present a theoretical model to explain this phenomenon. By determining the influence of supercoiling on the disruption barrier we demonstrate that torsion is crucial towards understanding the kinetics of nucleosome unwrapping.

3.1 Introduction

Genomic DNA in eukaryotic cells is highly organized. The fundamental packing unit is the nucleosome, where 147 base pairs of DNA are wrapped in 1.7 turns around a core histone octamer in a left-handed manner [72]. The crystal structure of a nucleosome core particle is shown in Figure 3.1. During DNA metabolism, motor proteins such as polymerases and topoisomerases must overcome

the barrier imposed by the nucleosome in order to perform their functions. Therefore, the dynamic nature of the nucleosome plays a critical role in gene regulation.

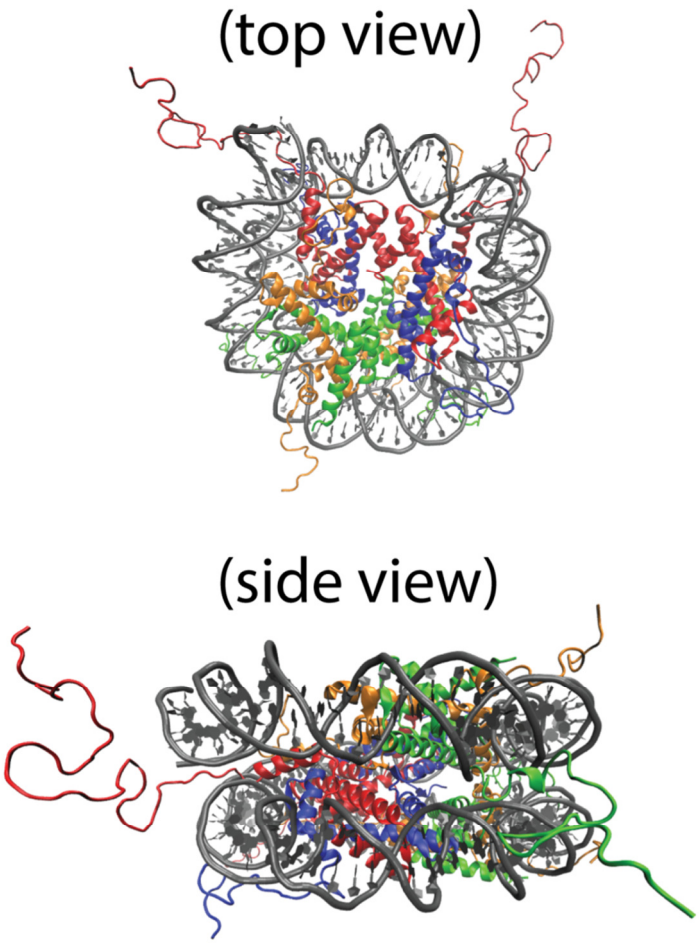

Figure 3.1: The crystal structure of nucleosome core particle (PDB code: 1KX5). 147 bp of DNA (gray) is wrapped around the histone octamer, which consists of two copies of H2A (orange), H2B (green), H3 (red) and H4 (blue). This figure is prepared using the software package: Visual Molecular Dynamics (VMD) [73].

Micromanipulation tools such as optical traps and magnetic tweezers have been applied to DNA molecules with multiple and single nucleosomes [74–79]. Applying force on a mononucleosome results in a multi-stage transition where a reversible unwrapping of 0.7 turns of DNA at lower force is followed by an

irreversible release of the remaining DNA at higher force [80,81]. The energy barrier for the second transition was measured to be 35 k_BT. This is unexpectedly high compared to the estimated net adsorption energy between histone proteins and DNA of 15 k_BT [82]. The relatively high energy barrier measured by the optical trapping experiments was later interpreted as an effect of the underlying geometry of the nucleosome [83,84].

While most of these experiments are without torsional constraint, nucleosomes *in vivo* are subject to both tension and torsion at the same time. The torsional state of chromosomal DNA can affect nearly all biological processes and it is natural to explore torsional effect on nucleosomes. Prior experiments using magnetic tweezers have addressed the torsional response of a chromatin fiber and revealed its structural plasticity [85,86]. However, all previous optical trapping experiments on nucleosomes allowed the DNA to rotate along its axis freely. Here, we carried out the first unwrapping experiments of a single nucleosome under torsional constraint using an optical torque wrench [53,59] and demonstrated that the kinetic barrier is sensitive to torsional manipulations in this biologically relevant context.

3.2 Material and Methods

3.2.1 DNA Template

The rotationally-constrained tether was ligated from three pieces of DNA made separately by polymerase chain reaction (PCR). As shown in Figure 3.2, the middle piece (1351 base pairs) contains a single 603 nucleosome positioning

sequence. Two short pieces randomly incorporate multiple digoxigenin (322 base pairs) and biotin (336 base pairs) labeled nucleotides, which allows for torsionally-constrained binding to the sample chamber surface and cylinder respectively. For experiments without torsion, the template DNA (1536 base pairs) with one 603 nucleosome positioning sequence was synthesized as one piece by PCR with digoxigenin and biotin labeled primers. Both kinds of DNA were phenol extracted before nucleosome reconstitution.

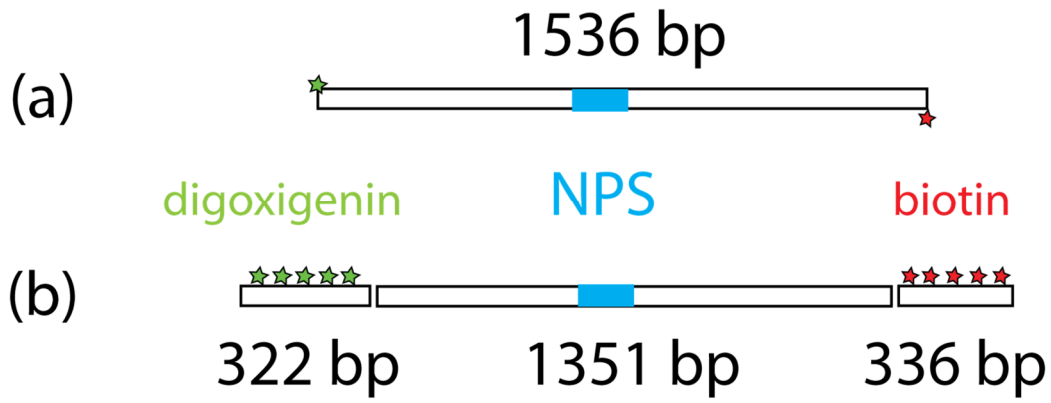

Figure 3.2: DNA template for single nucleosome unwrapping experiments without torsion (a) and with torsion (b). NPS: nucleosome positioning sequence.

3.2.2 Nucleosome Reconstitution

Chromatin donor was purified by Studitsky Lab[3]. The nucleosomes were reconstituted on the template DNA by stepwise salt dialysis [87,88]. Briefly, In order to obtain single nucleosome on one DNA template, the optimum chromatin:DNA weight ratio for reconstitution was determined empirically by ClaI enzyme restriction

[3] Collaboration with Vasily Studitsky, University of Medicine and Dentistry of New Jersey.

and gel mobility test (Figure 3.3). The reconstituted products were diluted right before injecting into sample chamber.

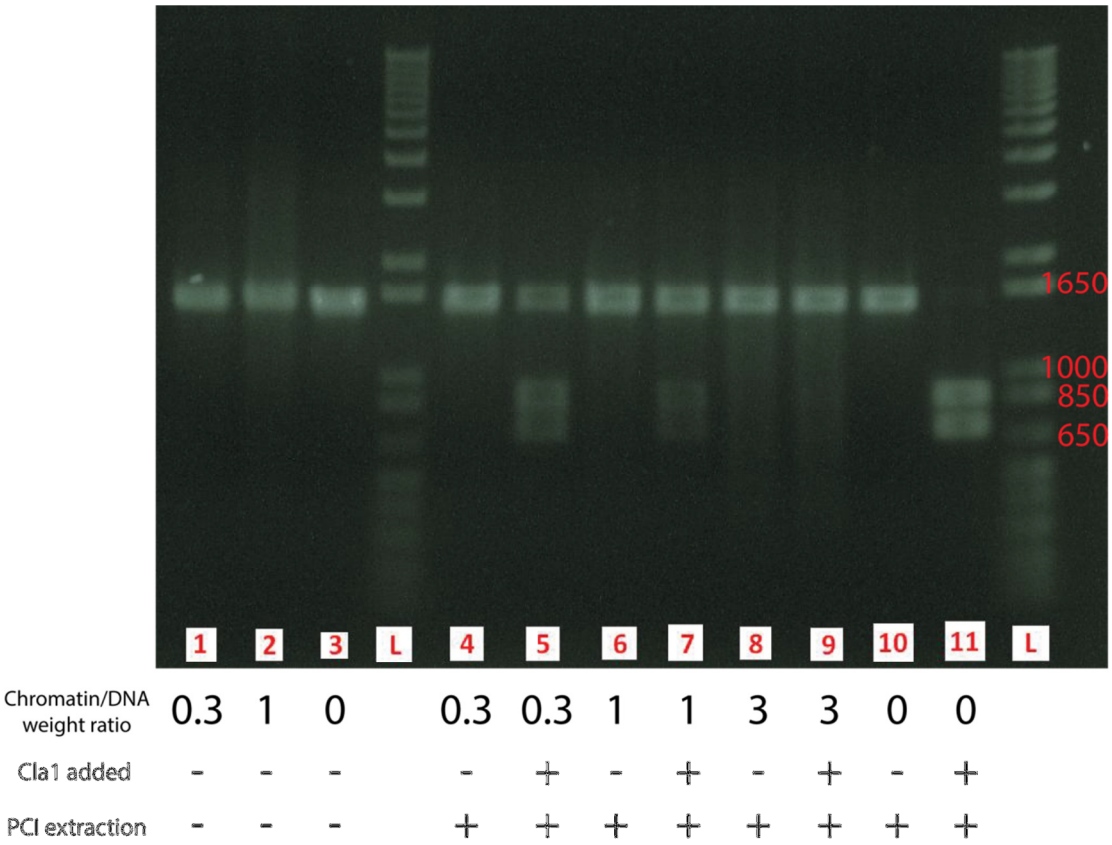

Figure 3.3: Determining optimal chromatin/DNA weight ratio for nucleosome reconstitution. L: 1kb plus DNA ladder.

All experiments were performed at 22 °C with final buffer conditions: 50 mM sodium phosphate buffer pH 7.0, 50 mM NaCl, 2mM $MgCl_2$, 0.02% Tween-20, and oxygen scavenger solution to protect the DNA from the laser damage.

3.3 Experimental Results

3.3.1 Nucleosome Unwrapping Without Torsion

We first disrupted nucleosome without torsional constraint as setup shown in Figure 3.4(b), i.e. no supercoiling can be built on the DNA. The typical force-extension curve is shown in Figure 3.4(b). Nucleosome undergoes two-stage transition when subject to end-to-end force: the outer 0.7 turns of DNA opens reversibly at lower force while the inner full turn of DNA unwraps irreversibly at higher force, as reported in the previous literature [80,81,89,90]. We measured the inner turn disrupting at 22.3±0.3 pN at force loading rate ~23 pN/s. This is comparable to chromatin fiber (multiple nucleosomes) pulling experiments [80,91,92], but slightly higher than other mononucleosome results [81,90], which may be attributed to various force increasing rates, histone octamer sources, positioning sequences, and buffer conditions used in the experiments.

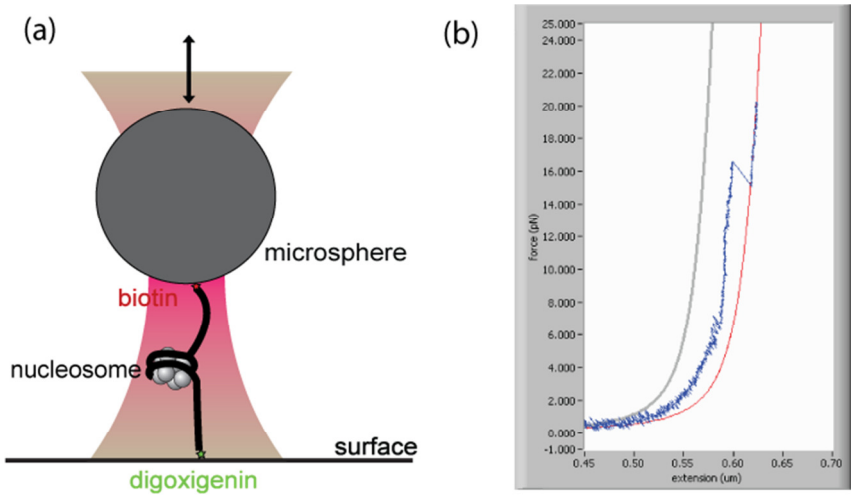

Figure 3.4: (a) Setup for disruption experiment without torsional constraint. (b) Typical force-extension curve.

3.3.2 Nucleosome Unwrapping With Torsion

We next conducted nucleosome experiments with rotationally-constrained DNA and optical torque wrench. Each molecule was initially stretched with no applied twist to determine if a single nucleosome was present. Then we applied positive and negative twists at constant linear force of 3 pN to verify that the tether was properly rotationally constrained (Figure 3.5). Once a validated tether was confirmed, it was given a prescribed twist without linear tension and then stretched with increasing force while constraining this fixed twist. Each molecule was stretched repeatedly at negative, zero, and positive twist with 5 seconds relaxation time between each scan. Supercoiling density σ, defined as twist turns * 3.52 nm / contour length of DNA, was used as a normalized quantity that specify the amount of torsional constraint added.

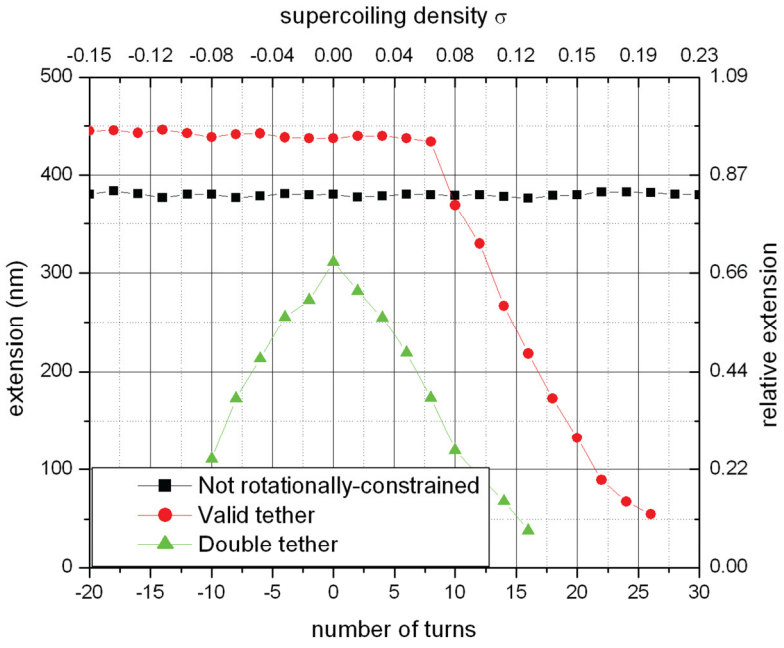

Figure 3.5: Verification of a properly rotational constrained DNA is achieved by measuring the rotation-extension curve at constant force 3pN.

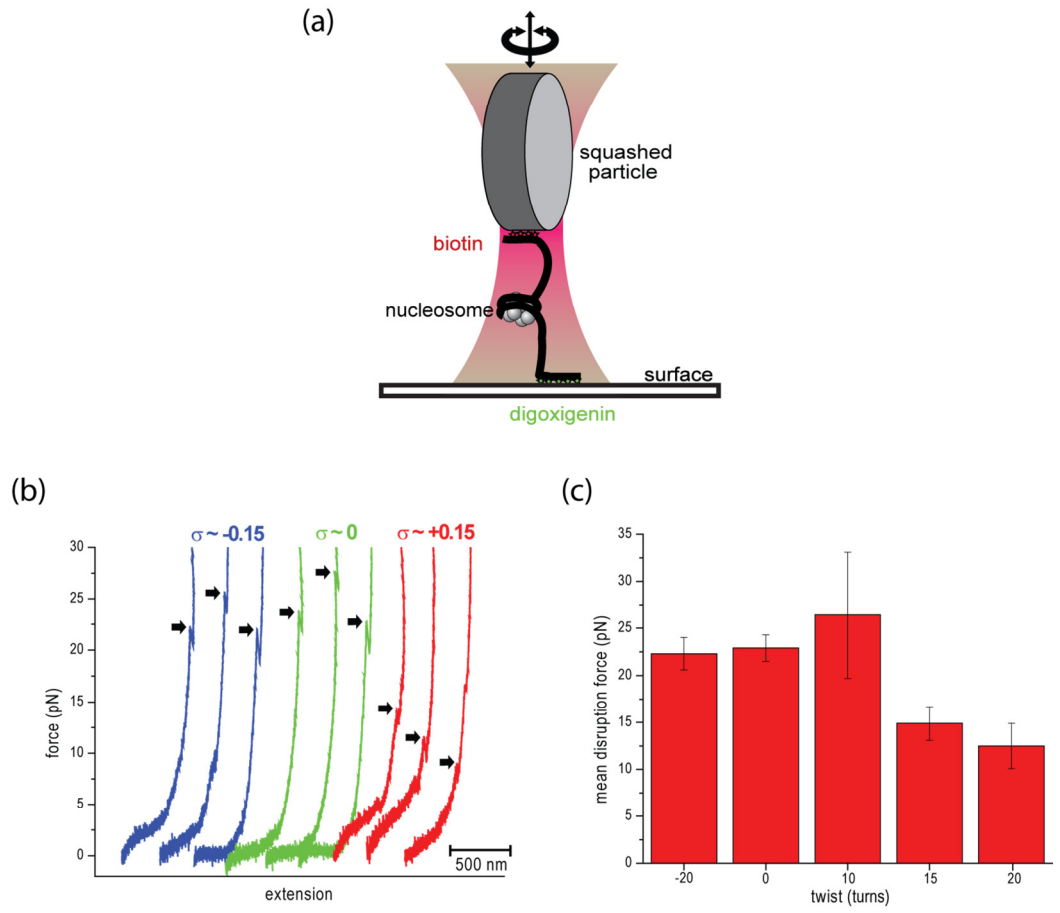

Figure 3.6: Effect of torsion on nucleosome disruption. (a) Experimental setup for nucleosome disruption with torsion. (b) Representative scans with different torsional constraint. Disruption events are identified by discontinuity on the force-extension curve as arrows indicate. Disruption force is lower with positive twist (red) but unchanged under negative twist (blue), comparing to no twist (green). (c) Disruption force (mean ± s.d.o.m.) as a function of twist turns added.

Figure 3.6(b) shows the resulting force-extension curves at negative, zero, and positive twist. We focused on the inner turn transition which is indicated by the arrows on each curve. With no twist (green curve), disruption of the nucleosome occurred at force 25±2 pN, identical with experiments without torsional constraint. With large enough positive twist (σ ~ +0.15) disruption force was significantly lower to 14±2 pN or unidentified. Negative supercoiling (σ ~ -0.15) resulted in a mean disruption force which was indistinguishable from no supercoiling. Figure 3.6(c) shows the mean disruption force as a function of twist added.

3.4 Theoretical Modeling

To further quantify the effect of torsional constraint on nucleosome stability, we developed a model of the energy landscape for the system E_{sys} containing the contribution from nucleosome E_{nuc} and the flanking DNA E_{fl}. It is a function of DNA desorption angle α (α = 0 for one full turn of wrapped DNA and α = π when the DNA is fully unwrapped), histone tilt angle β (β = 0~π), and experimental controllable parameter force F, and supercoiling density σ.

$$E_{sys}(\alpha, \beta; F, \sigma) = E_{nuc}(\alpha, \beta; F) + E_{fl}(F, \sigma) \quad (3.1)$$

The total energy of the nucleosome part are treated as DNA adsorbed on a spool surface along a predefined helical path [83]. It can be decomposed into three terms:

$$E_{nuc} = E_{comp} + E_{geom} + E_{stiff} \quad (3.2)$$

where E_{comp}, E_{geom}, and E_{stiff} describe the competition of the adsorption and the applied force, the geometrical energy stems from the gain or loss of potential energy

by spool opening and rotation, and the stiffness of the desorbed DNA, respectively. Specifically,

$$\begin{aligned} E_{comp}(\alpha;F) &= 2R(\mu_{ads}-F)\alpha \\ E_{geom}(\alpha,\beta;F) &= 2FR\left[\cos\beta\sin\alpha+\frac{H}{2\pi R}(\pi-\alpha)\sin\beta\right] \\ E_{stiff}(\alpha,\beta;F) &= 8\sqrt{BF}\left[1-\sqrt{\frac{1}{2}\left(1+\frac{R}{\bar{R}}\cos\beta\cos\alpha+\frac{H}{2\pi\bar{R}}\sin\beta\right)}\right] \end{aligned} \quad (3.3)$$

R is the radius and H is the pitch height for the helical path of the DNA around nucleosome, μ_{ads} is the adsorption energy density for the DNA-histone interaction, B is the DNA bending stiffness at room temperature, and $\bar{R}^2 = R^2 + \frac{H^2}{4\pi^2}$. This model agrees nucleosome stretching experiments without torsional constraint and explained some of the discrepancy between data from biochemistry assays and single-molecule experiments.

The energy for flanking DNA employed a phenomenological model accounting DNA phase transition under force and torque [64,65,68]. Under the combination of torsion and tension, one or more of the following DNA states are assumed to be coexisted: L-DNA (favored when subjecting to large negative twist), B-DNA, and supercoiled state (sc-DNA, favored when subjecting to large positive twist). The energy of the flanking DNA can be expressed as

$$E_{fl}(F,\sigma) = L\sum_i G_i(F,\sigma)x_i \quad (3.4)$$

where L is the length of DNA, G_i is the free energy density for each state, and x_i is the fraction of each state. (i = B, L, or sc stands for B-DNA, L-DNA or supercoiled state) For each state, the energy density G_i can be approximated as

$$G_i(F,\sigma) = \varepsilon_i - g_i(F) + \frac{1}{2}c_i(f)(\sigma - \sigma_{0,i})^2 \quad (3.5)$$

where ε_i is the energy offset, and $\sigma_{0,i}$ is the relaxed degree of supercoiling for the state. $g_i(F)$ and $c_i(f)$ are stretching energy and torsional coefficients as a function of force which can be derived from polymer theory:

$$\begin{aligned} g_i(F) &= b_i\left(F - \sqrt{\frac{k_B T F}{A_i}} + \frac{F^2}{2K_i}\right) \\ c_i(f) &= k_B T C_i \omega_0^2 \left(1 - \frac{C_i}{4A_i}\sqrt{\frac{k_B T}{A_i F}}\right) \end{aligned} \quad (3.6)$$

where A_i is the persistence length, C_i is the torsional modulus, K_i is the stretch modulus and b_i is the contour length ratio to that of B-DNA for each state. $\omega_0 = 2\pi/3.6nm$ is the contour-length rate of rotation of the relaxed double helix.

parameter	value	unit	parameter	value	unit
R	4.2	nm	H	2.4	nm
B	50	$k_BT \cdot nm$	μ_{ads}	$0.7 + 1.7\theta(\alpha)^4$	k_BT/nm
ε_B	0	k_BT/nm	$\sigma_{0,B}$	0	-
A_B	43	nm	K_B	1200	pN
C_B	95	nm	b_B	1	-
ε_L	6.25	k_BT/nm	$\sigma_{0,L}$	-1.6	-
A_L	5.5	nm	K_L	0	pN
C_L	17	nm	b_L	1.37	-
ε_{sc}	0	k_BT/nm	$\sigma_{0,sc}$	0	-
C_{sc}	24	nm	b_{sc}	0	-

Table 3.1: Parameter values used for modeling nucleosome unwrapping energy landscape.

[4] The step function accounts the DNA-DNA repulsion of the two adjacent helical gyres which acts only for more than one turn present.

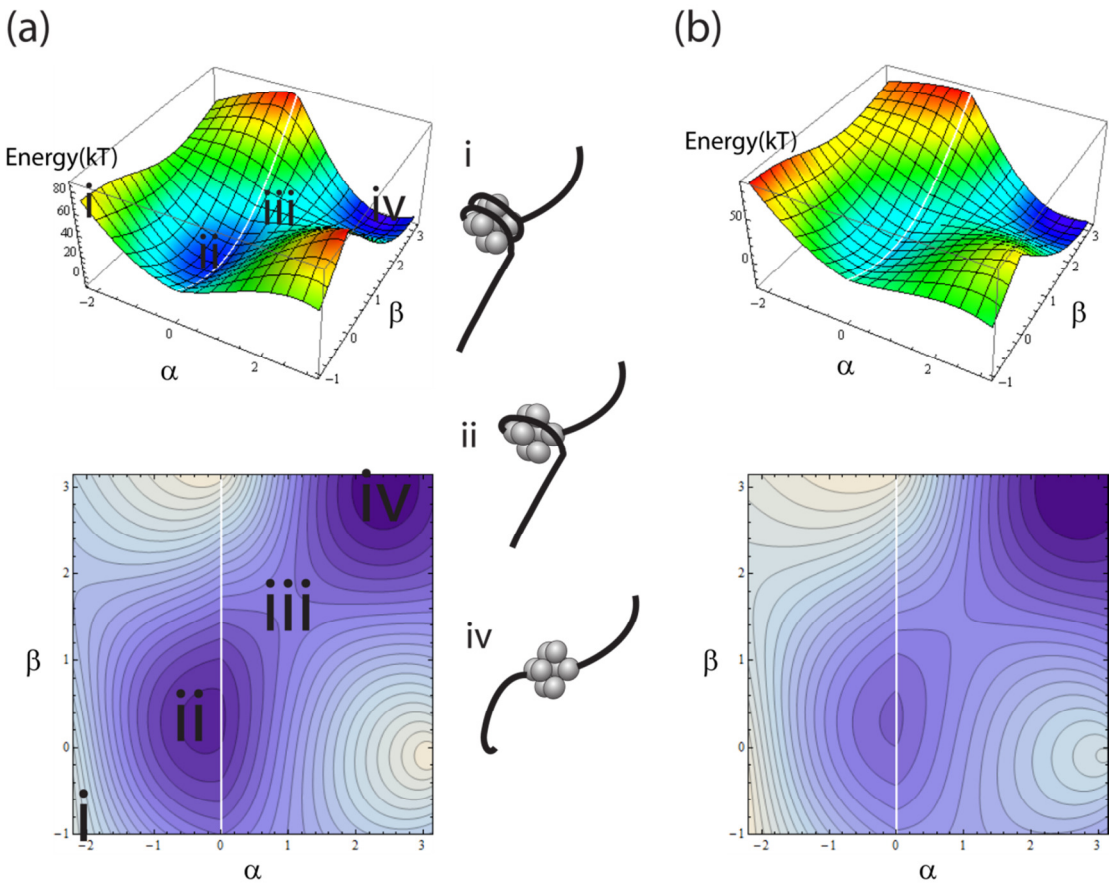

Figure 3.7: Energy landscape for nucleosome disruption. Both 3d surface (top) and contour plots (bottom) are shown for modeled energy landscape for the system under force 10pN and twist (a) 0 and (b) +10 turns. The inner turn transition when mechanically disrupting a nucleosome is equivalent to a Brownian particle diffusing from state ii to iv on this force- and twist-dependent energy surface. The transition barrier height (energy difference in state iii and state ii) is lowered due to the effect of twist.

For a given set of force and twist, we now have an expression for the total energy of the system as a function of α and β. Figure 3.7 plots an example, the total energy is sensitive to the twist applied under the same tension. The parameter values used are listed in Table 3.1: Parameter values used for modeling nucleosome . Our stretching experiment is equivalent to a Brownian particle diffusing on this force- and twist-dependent two dimensional energy surface. We define the barrier height for the second unwrapping transition as the energy difference between the initial state (state ii on Figure 3.7(a), local minimum near $(\alpha,\beta) = (0,0)$) and the saddle point connecting initial and final state (state iii on Figure 3.7(a), local minimum near $(\alpha,\beta) = (\pi,\pi)$).

We now consider how twist affects the energy barrier height. Figure 3.8 plots effective barrier height as (a) a function of force under different twist and (b) a function of twist under various constant forces. Note that under constant force, barrier height is lowered at large positive twist while remain constant for negative twist. This is consistent with our experimental results.

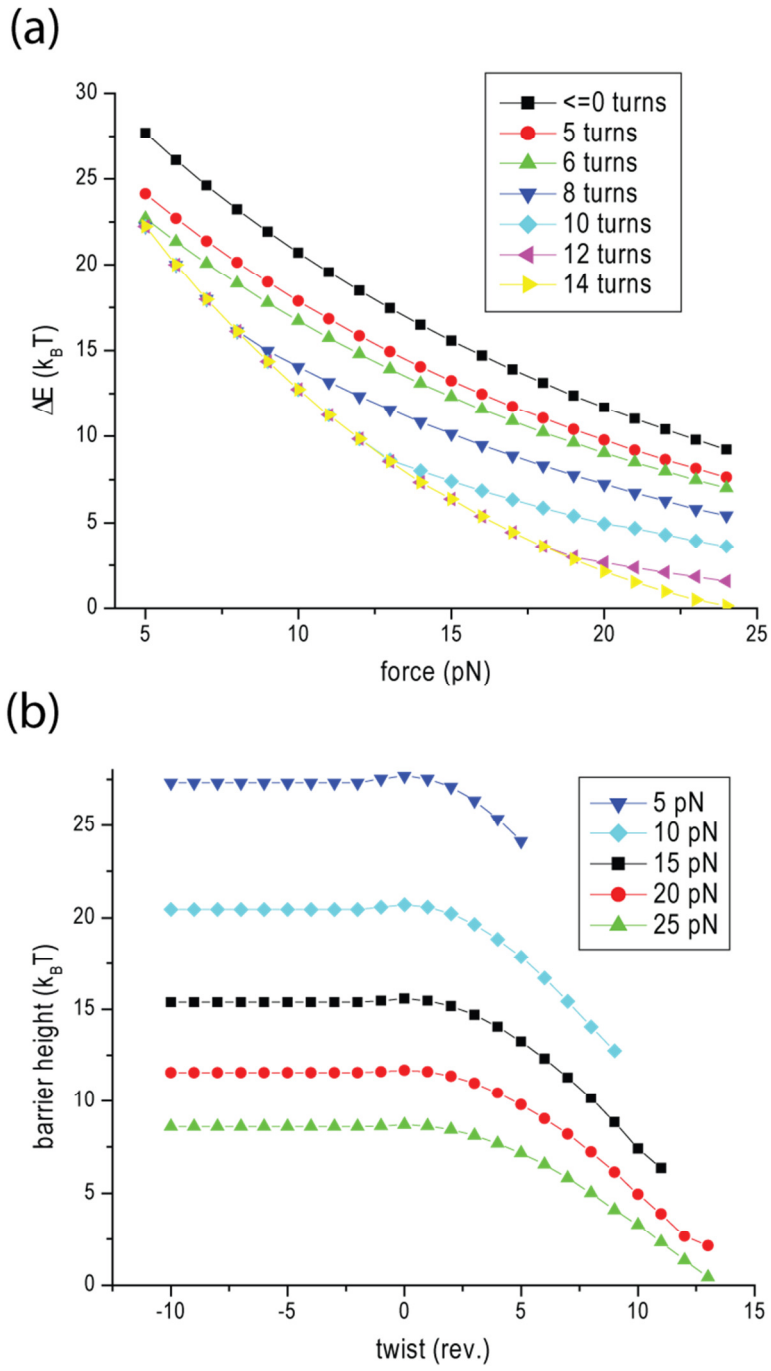

Figure 3.8: Modeled energy barrier height is sensitive to torsion. The prediction of the effective barrier height as a function of (a) force and (b) twist. The barrier height is lowered when subjecting to positive twist while remaining constant for negative twist, consistent with experimental observation.

3.5 Discussion and Conclusion

Our result provided another view to the long standing questions that nucleosome poses a huge barrier that seems impossible for a motor protein to overcome, while it must be accessible to be processed in the cell. Kulic and Schiessel's model provided an explanation that the second turn of DNA is much weakly bound to the histone due to the electrostatic DNA-DNA repulsion [83,84]. As long as the first turn of DNA is desorbed and absorbed in a consistent manner, there is no extra energy for the protein to progress. Therefore, the DNA deep inside the nucleosomes can be accessed easily despite the high energy barrier. On the other hand, our work suggests that the barrier height measured by previous pulling experiments without torsional constraint may not represent the biologically relevant situation.

The fact that torsional constraint effectively lowers the nucleosomal barrier height can be put into cellular context. During transcription elongation, positive (negative) supercoiling is generated downstream (upstream) of an RNA polymerase [93]. Recent *in vivo* studies have also shown the importance of transcription-dependent dynamic supercoiling to gene regulation [94–96]. According to our data, we propose a scheme that the twist generated by the DNA motor protein itself can destabilize the nucleosome and facilitate the subsequent DNA transaction. Moreover, the speed for propagation of positive torsional stress may be one of the factors that regulate the transcription.

In our present analysis, one must bear in mind that the nucleosome is assumed not undergoing structural transitions. However, chromatin state *in vivo* is highly

dynamic in both its extent of DNA wrapping or the composition and stoichiometry of core particle [97]. Recent magnetic tweezers experiment proposed that under large positive torsional stress a canonical left-handed nucleosome can make a chiral transition to a metastable righ-handed form (termed reversome) [86]. This indicates that molecule we stretch under positive supercoiling may be reversome. In any case, this does not change our conclusion that positive torsion destabilizes canonical nucleosomes.

We also note that for the data with torsion only those molecules that can be stretch repeatedly with at least a cycle of zero, negative and positive supercoiling are presented, which represents less than 20%. Most molecules exhibited no disruption for the stretch following ones with positive twist, indicating complete or partial histone loss. Additionally, with positive supercoiling, some disruption broke into several steps (right most curve in Fig). We associate these observations to hexasome or tetrasome formation during polII transcription reported in previous literature [98–100], and proposed that the various torsional state on DNA is one of the physical mechanism for H2A/H2B dimer loss which is one of the key factor for gene regulation.

In this chapter, we conducted nucleosome unwrapping experiments, with torsional constraints for the first time, and demonstrated that the disruption force is significantly lowered if large enough torsion was constrained, while negative supercoiling does not alter the disruption force. An analytical model was also developed and found to be consistent with our experimental data. Our result demonstrates that torque is a crucial parameter towards understanding the mechanical

stability of the nucleosome, which has regulatory implications. Our work naturally leads to other single-molecule experiments to explore the torsional effect on histone-DNA interactions with histone tails, histone variants, and other chemical modifications.

Chapter 4:Effect of handle length and microsphere size on transition kinetics in single-molecule experiments[5]

When subject to constant tension, a DNA or RNA hairpin will typically make abrupt transitions between the open and closed state. Although the transition kinetics are an intrinsic property of the molecule, the transition rates measured in single-molecule experiments can be influenced by the configuration of the measurement system. In this chapter, we investigate the transition kinetics for a DNA hairpin held under constant force by an optical trap as a function of microsphere size and double-stranded DNA handle length. We find the apparent transition lifetime cannot be expressed as a function of the drag coefficient of the microsphere alone or as a function of time scales relevant to the optical trap. The apparent transition lifetime is found to be a linear function of the factor $\beta_{\text{eff}} \cdot \alpha_{\text{handle}}$, where β_{eff} is the effective drag coefficient of the microsphere near the surface and α_{handle} is the stiffness of the DNA tether. The results provide insight into the perturbation to the hairpin transition kinetics due to experimental configuration and guidance for designing single-molecule experiments which determine the intrinsic molecular kinetics.

4.1 Introduction

Single-molecule techniques such as optical traps, magnetic tweezers, and atomic force spectroscopy, are powerful tools for exploring the kinetics of bio-molecules. Force is generally applied to a single molecule construct via linked

[5] This chapter is partially adapted from [101].

'handles' – usually double stranded DNA or DNA-RNA hybrid – which connect the two ends of the construct to a force transducer. The molecular construct may be tethered between a surface and a trapped microsphere or magnetic particle, or may be tethered between two particles. In our study a DNA hairpin is tethered between a surface and a trapped microsphere (Figure 4.1). In the absence of applied force, the folded conformation of the molecule typically has lower free energy and is thermodynamically favored. Applied force biases the equilibrium towards the unfolded conformation (Figure 4.2(a)), and transitions between the folded and unfolded conformation can be detected by tracking the microsphere.

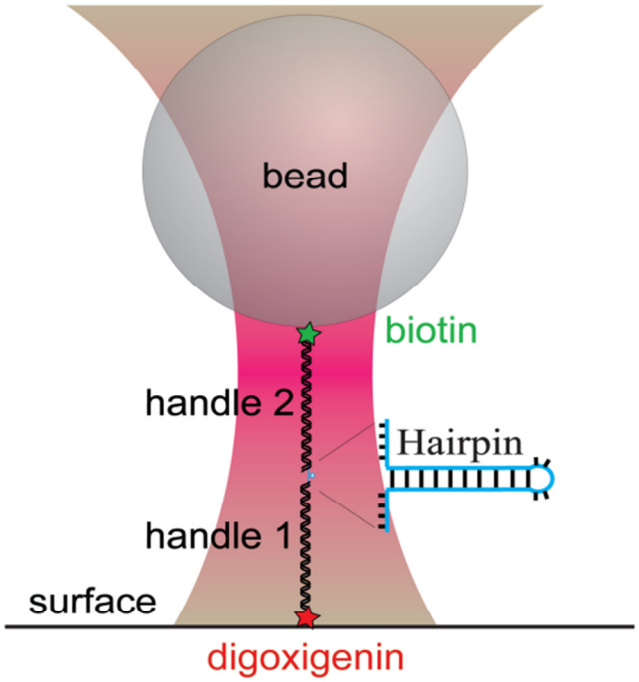

Figure 4.1: Experimental setup. The molecule is stretched in the axial direction of laser beam.

Aside from modifying the relative stability of the folded and unfolded conformations, the attachments to the molecule can have a complex effect on the

transition kinetics. Transitions between different conformations are driven by thermal fluctuations and the fact that handles have been attached to the molecule may hamper its intrinsic conformational dynamics. The presence of the trapped microsphere can also subject the molecule to additional drag and fluctuations. Experimental factors such as force field stiffness, force mode (passive or force-clamped), feedback bandwidth, handle lengths, and viscous drag on the microsphere can therefore affect the rate at which the molecule is observed to fluctuate between conformations, making extraction of the intrinsic kinetics of the molecule difficult [102–105].

Among these factors, handle length is of particular interest because it can be varied over two orders of magnitude. The best long term stability has been obtained from a geometry in which the molecule is tethered between two microspheres held in separate optical traps, which requires a total tether length of several thousand base pairs [102]. In contrast, Forns et al. demonstrated that the signal/noise ratio for extension measurement is improved by the use of very short handles (totaling 58 base pairs) [105], which is consistent with theoretical and experimental results indicating that the energy landscape is measured with higher resolution when shorter handles are used [17,106].

Previous theoretical and experimental results showed that the transition rate of a hairpin can be influenced by handle length [103–106]. In the limit that there is a clear separation of time scales between the dynamics of the hairpin and those of the microsphere, Hyeon et al. found that the theoretical transition rates for a hairpin are reduced by the presence of the handles and that shorter handles minimize this effect

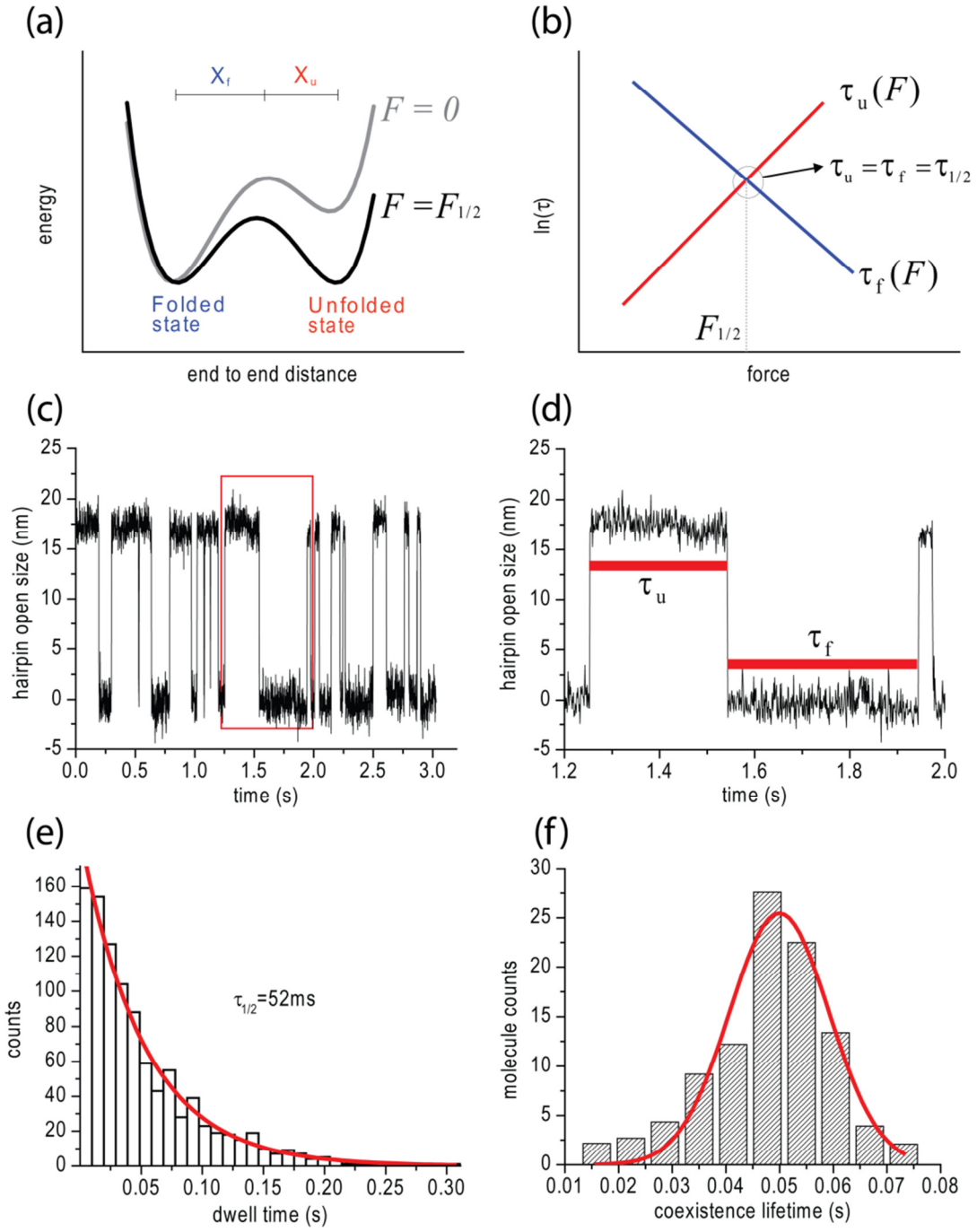

Figure 4.2: Concept and analysis for coexistence lifetime. (a) Energy landscape for a typical two-state folder. (b) Definition of coexistence lifetime. (c) Representative trace of data for total handle length 1224 bp. (d) Zoom-in plot of boxed region in (c). (e) Fitting overall dwell time distribution to an exponential function gives coexistence lifetime for a single molecule. (f) A Gaussian fit to the lifetime distribution for all molecules with total handle length 1224 bp.

[106]. However, an experimental study in a different regime of experimental parameters found a faster transition rate for longer handles than for shorter ones [105].

Here we report an extended experimental study in which we characterize the extent to which the single-molecule measurement system perturbs the transition kinetics of a DNA hairpin. In this study we vary the handle length L and microsphere radius R, while keeping other properties of the measurement system, such as the force clamp feedback loop, the intrinsic stiffness of the optical trap, the surface-based experimental configuration and the solution temperature and viscosity, constant. Since the transition kinetics are not known *a priori* it is not possible to determine the absolute amount by which the measurement system perturbs the transition kinetics. However, it is possible to determine how the perturbed transition kinetics depend on L and R. As we will describe below, we find that the apparent transition lifetime is determined by the product of the effective drag coefficient of the microsphere and the coupling strength between the molecule and the microsphere. The apparent transition lifetime approaches an asymptotic value as the microsphere drag vanishes, or as the coupling becomes weak.

4.2 Materials and methods

4.2.1 Sample preparation

DNA hairpins (sequence gagtcaacgtctggatcctgttttcaggatccagacgttgactc) were prepared as described in our previous work [17] except that double-stranded DNA handles were produced with lengths of 1030, 347, or 234 base pairs on the microsphere side (biotin-labeled) and 2686, 1402, 569, 194, or 100 base pairs on the

surface side (digoxigenin-labeled). The ligated products were chosen to contain total handle length of 428, 803, 916, 1130, 1224, 1502, 1599, 1636, 2432, or 3716 base pairs. Two different microspheres (Bangs Laboratories, Inc., Fishers, IN) with radii 255 nm and 410 nm were used.

Experiments were conducted with 50 mM sodium phosphate buffer pH 7.0, 50 mM NaCl, 10 mM EDTA, 0.02% Tween 20, and oxygen-scavenging solution for protection from optical damage (721 mg/ml glucose oxidase (Sigma, St. Louis, MO), 144 mg/ml catalase (Sigma), and 3.9 mg/ml glucose) [107].

4.2.2 Optical trapping method and data analysis

Since the model hairpin is essentially a two-state folder with first-order kinetics, at a given force *F*, the probability that the molecule will dwell in the folded ($P_{\mathrm{f}}(t,F)$) or unfolded ($P_{\mathrm{u}}(t,F)$) conformation for time *t* follows an exponential relation,

$$P_{\mathrm{f}}(t,F)=\exp\left(\frac{-t}{\tau_{\mathrm{f}}(F)}\right),\quad P_{\mathrm{u}}(t,F)=\exp\left(\frac{-t}{\tau_{\mathrm{u}}(F)}\right), \tag{4.1}$$

where $\tau_{\mathrm{f}}(F)$ and $\tau_{\mathrm{u}}(F)$ are the mean lifetimes of the folded and unfolded states. In addition, $\tau_{\mathrm{f}}(F)$ and $\tau_{\mathrm{u}}(F)$ depend exponentially on the force *F* [29,30],

$$\tau_{\mathrm{f}}(F)=\tau_{\mathrm{f}}(0)\exp\left(\frac{-FX_{\mathrm{f}}}{k_{\mathrm{B}}T}\right),\quad \tau_{\mathrm{u}}(F)=\tau_{\mathrm{u}}(0)\exp\left(\frac{-FX_{\mathrm{u}}}{k_{\mathrm{B}}T}\right) \tag{4.2}$$

where $\tau_{\mathrm{f}}(0)$ and $\tau_{\mathrm{u}}(0)$ are the intrinsic lifetimes at zero force, X_{f} and X_{u} are the distances from the folded or unfolded state to the transition state along the reaction coordinate (end to end extension of the hairpin in this case), k_{B} is the Boltzmann

constant, and T is the temperature. If $F_{1/2}$ is the force such that the hairpin has equal probability of occupying the folded or unfolded conformation, then we can define the coexistence lifetime as $\tau_{1/2} \equiv \tau_{\mathrm{f}}(F_{1/2}) = \tau_{\mathrm{u}}(F_{1/2})$ (Figure 4.2(b)) [108]. The trap intensity is controlled by an acousto-optic modulator (AOM) and the value of $F_{1/2}$ was determined by adjusting the trap intensity to obtain equal probabilities of being in the folded and unfolded conformation. Constant force at $F_{1/2}$ (force clamp) was implemented using feedback to the trap intensity. Slow feedback on the piezo-stage position compensated for surface drift by requiring that the probability of occupying either state is between 40 – 60 % in a 10-15 s time window. The average trap power was constant during measurements. The nominal stiffness of the optical trap without the force clamp would be 0.05 pN/nm. Other details of the optical trapping apparatus and calibration have been described elsewhere [17].

Data were taken at 20 kHz or 10 kHz for ~150 s per molecule (>500 transitions) and boxcar filtered to 1 kHz for analysis. A representative trace of the data is shown in Figure 4.2(c) and (d). The hairpin total opening size is determined by the distance between the two peaks of double Gaussian fit to the extension distribution. A transition is identified when the hairpin extension crosses the half-way point (~9 nm). The filtering of the data ensures that noise in the extension measurement does not result in detection of spurious transitions. The dwell time is the time difference between an opening and closing transition, or vice versa. For each molecule, $\tau_{1/2}$ was determined by fitting the combined dwell time distribution to Eq. 4.1 (Figure 4.2(e)). For each set of handle lengths, 25-100 molecules were measured in 1-4 sample chambers. For each sample chamber, $\tau_{1/2}$ was determined as the mean

of the Gaussian fit to the distribution of $\tau_{1/2}$ (Figure 4.2(f)). In cases where all molecules were collected on a sample chamber, the result of this Gaussian fit is reported. In cases where more than one sample chamber was used, the average of the Gaussian fits is reported. Total uncertainty includes contributions from the statistical uncertainty of the Gaussian fits and systematic calibration error, estimated to be ~10%. Below, we consider the dependence of $\tau_{1/2}$ on handle length and microsphere radius.

4.3 Result and discussions

4.3.1 Coexistence lifetime is correlated with the total handle length

First we consider how the total handle length influences the measured coexistence lifetime. The red circles in Fig. 4.3(a) show that $\tau_{1/2}$ decreases 3-fold for the 410 nm radius microsphere, as the total handle length was increased 4-fold. The black squares in Fig. 4.3(a) show that $\tau_{1/2}$ decreases 2-fold for the 255 nm radius microsphere, as the total handle length was increased 9-fold. For a given microsphere radius, the coexistence lifetime depends on the total handle length, The trend that measured coexistence lifetimes get longer as handles are made shorter is qualitatively consistent with recently reported results [105]. Our results also demonstrate that the measured coexistence lifetime approaches an asymptotic value which is independent of the microsphere radius in the limit of very long handles. However, for short handles, the lifetime depends on the microsphere size, as we discuss below.

The DNA hairpin used in this study is identical to that used by Woodside *et al* [15]. The value of $\tau_{1/2}$ we measured using 1,636 base pairs handles (52 ± 5 ms) is consistent with their result (55 ± 17 ms) despite the different experimental configuration employed by Woodside et al. (double-beam trap with intrinsic force clamp and somewhat different buffer conditions). This is consistent with the assumption that in the limit of long handles, the measured kinetics is not sensitive to drag on the microspheres and trap stiffness.

H1 (bp)	H2 (bp)	Total (bp)	L (nm)	α_{handle} (pN/nm)	τ_b (μs)	β_{eff} ($6\pi\eta$·nm)	$\tau_{1/2}$ (ms)	R (nm)	N
194	234	428	140	2.88	10.56	1640	162 ± 16	410	52
569	234	803	263	1.53	13.07	1100	104 ± 11	410	112
569	347	916	300	1.34	13.75	1020	91 ± 9	410	112
100	1030	1130	369	1.09	15.02	908	60 ± 6	410	88
194	1030	1224	400	1.01	15.54	872	59 ± 6	410	98
1402	100	1502	491	0.820	17.12	789	55 ± 6	410	73
569	1030	1599	523	0.770	17.64	767	52 ± 5	410	68
1402	234	1636	535	0.753	17.84	759	52 ± 5	410	62
194	234	428	140	2.88	4.75	738	92 ± 9	255	35
569	234	803	263	1.53	6.25	524	66 ± 7	255	36
194	1030	1224	400	1.01	7.77	435	53 ± 5	255	25
569	1030	1599	523	0.770	9.06	394	45 ± 5	255	25
1402	1030	2432	795	0.506	11.76	347	45 ± 5	255	23
2686	1030	3716	1220	0.331	15.60	315	40 ± 4	255	22

Table 4.1: List of data for all handle lengths and microsphere sizes. H1: length of handle connected to the surface. bp: base pairs. H2: length of handle connected to the microsphere. Total: total handle length. L: extension of handle at 13.2 pN. τ_b : microsphere relaxation time. β_{eff}: effective drag coefficient. $\tau_{1/2}$: coexistence lifetime. R: microsphere radius. N: number of molecules.

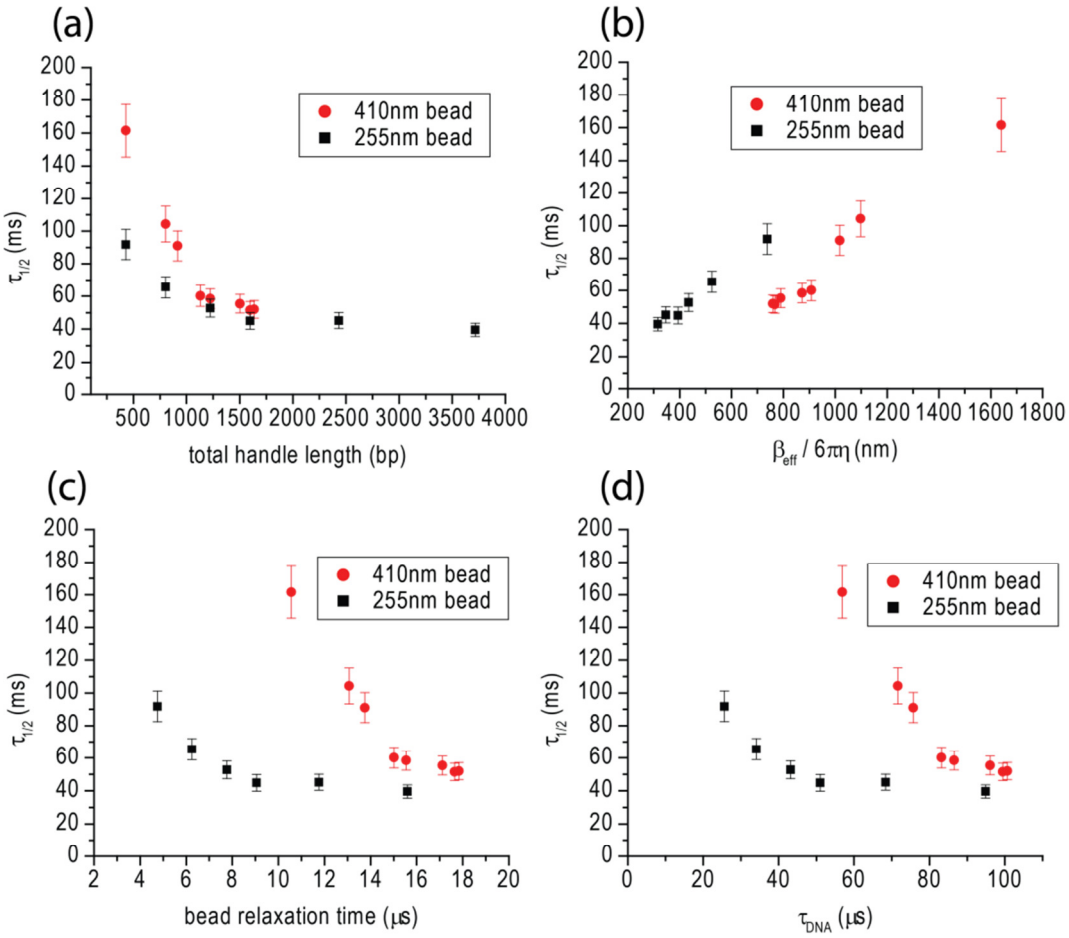

Figure 4.3: Coexistence lifetime $\tau_{1/2}$ of hairpins for various combinations of microsphere radius and handle length. (a) $\tau_{1/2}$ as a function of handle length for two microsphere radii. (b) $\tau_{1/2}$ as a function of effective drag coefficient. (c) $\tau_{1/2}$ as a function of microsphere relaxation time τ_b including the effect of the handles. (d) $\tau_{1/2}$ as a function of the relaxation time accounting for DNA tether only.

4.3.2 Coexistence lifetime is correlated with the microsphere size

Now we consider how the kinetics depends on the microsphere radius. Comparing the data for 410 nm and 255 nm microspheres in Fig. 4.3(a), for the same handle length, the coexistence lifetime obtained for the large microsphere is longer, but the difference becomes negligible as the handle length increases. The fact that the

lifetime is longer for the larger microsphere suggests that drag on the microsphere impedes the transition kinetics, and the loss of sensitivity to the microsphere size with long handles can be attributed to the fact that the stiffness of the linkage between the microsphere and hairpin decreases with the handle length. It is apparent that neither the handle length nor the microsphere size is in itself sufficient to determine how much the coexistence lifetime is perturbed by the measurement system, but that the observed lifetime depends on both quantities.

4.3.3 Relationship of coexistence lifetime with properties of the optical trapping assay

We first consider whether the perturbation to the lifetime is dominated by one of the physical parameters of the measurement system. One possibility suggested above is that the drag on the microsphere impedes the hairpin folding dynamics, reducing the transition rate. For a sphere in an infinite fluid volume the drag coefficient is given by the Stokes law, $\beta = 6\pi\eta R$, where η is the viscosity and R is the radius. However, when the microsphere approaches the surface the effective drag coefficient increases, and this could explain the fact that the coexistence lifetime gets longer as the handle length is reduced. The effective drag coefficient for a sphere near a planar surface is $\beta_{\text{eff}} = 6\pi\eta R g$, where g is the surface correction factor, which is given as a function of the height h of the microsphere center relative to the surface by Schäffer *et al*. [109],

$$g\left(\frac{h}{R}\right) = \left(1 - \frac{9}{8}\left(\frac{h}{R}\right)^{-1} + \frac{1}{2}\left(\frac{h}{R}\right)^{-3} - \frac{57}{100}\left(\frac{h}{R}\right)^{-4} + \frac{1}{5}\left(\frac{h}{R}\right)^{-5} + \frac{7}{200}\left(\frac{h}{R}\right)^{-11} - \frac{1}{25}\left(\frac{h}{R}\right)^{-12}\right)^{-1},$$

The height h is related to the length L of the tether by $h/R = L/R + 1$. For large L/R, the correction factor approaches 1 and as L/R approaches zero $g \approx R/L$. In Fig. 4.3(b) we plot the coexistence lifetime $\tau_{1/2}$ as a function of the effective drag coefficient β_{eff}, where the nominal tether length L is determined by applying the worm-like chain model to the handles, with $F_{1/2} = 13.2$ pN [15]. It is clear that the two microsphere diameters produces a distinct curves of $\tau_{1/2}$ vs β_{eff}. This means that configurations with the same value of β_{eff} produce different values of $\tau_{1/2}$, depending on the microsphere radius. The perturbation to the coexistence lifetime is not determined by β_{eff}.

The drag on the DNA handles themselves may also be a factor that affects transition kinetics of the hairpin. In the high force regime the handles may be modeled as rigid rods, allowing the drag coefficient β_{handle} to be approximated as that of a cylinder in a steady axial flow at low Reynolds number. This gives $\beta_{\text{handle}} = 4\pi\eta L / (\ln(L/d) + 2\ln(2) - 0.5)$ [110], where d ~ 2 nm is the effective diameter of double-stranded DNA. This predicts a drag coefficient which increases with L and which is 3 to 90 times smaller than that the drag coefficient of the microsphere in our experimental configurations. Drag on the handles is excluded as the dominant perturbation of the transition kinetics by the small value of the DNA drag coefficient relative to the microsphere and by the fact that the observed hairpin dynamics get faster (not slower) as L increases.

Another hypothesis is that the coexistence lifetime is affected by a timescale associated with the optical trapping assay. For small displacement of the microsphere from its equilibrium position the microsphere will be subject to a linear restoring

force characterized by a stiffness α and will return to the equilibrium position with relaxation time $\tau_f = \beta_{eff}/\alpha$. If we take α to be the stiffness of the optical trap, the time scale we obtain is the free microsphere relaxation time τ_f. Since the trap stiffness is the same for all data runs, τ_f is proportional to β_{eff}. Therefore Fig. 4.3(b) also shows that the perturbation to $\tau_{1/2}$ by the measurement system is not determined by τ_f. If we assume that the feedback loop stabilizing the force on the microsphere is slow compared with the dynamics of the hairpin, the relevant relaxation time τ_b for the tethered microsphere would be one where α is taken to be the combined stiffness of the trap and of the DNA handles (where the dependence of the stiffness on the handle length is taken into account) [111]. As plotted in Fig. 4.3(c), it is clear that the effective $\tau_{1/2}$ cannot be expressed as a function of τ_b. If the force feedback is assumed to be fast compared with the hairpin dynamics the effective trap stiffness would be zero, and the relevant time scale τ_{DNA} would be one where the stiffness is given by the DNA tether alone. As shown in Fig 4.3(d), the effective $\tau_{1/2}$ cannot be expressed as a function of this time scale either.

4.3.4 Coexistence lifetime is determined by the combination of microsphere drag and tether stiffness

In the section above, we concluded that the perturbation to the transition kinetics by the optical trap could not be explained in terms of the microsphere drag coefficient or in terms of one of the characteristic time scales of the measurement system. However, the fact that the transition rate observed for a given tether length slowed when the microsphere size was increased suggests that the drag on the bead is

important. The fact that the observed transition rate approached an asymptotic value as the handle length L was increased suggests that long handles can isolate the hairpin from the influence of the microsphere. In view of these observations, we plot the coexistence time as a function of the product of effective microsphere drag coefficient β_{eff} and the handle stiffness α_{handle} at the coexistence force. Here α_{handle} is meant to parameterize how strongly the hairpin 'feels' the drag of the microsphere. Modeling the DNA handle as an elastic rod, the stiffness at a given force is given by A_0E/L, where A_0E is the product of the effective cross-sectional area and Young's modulus, so that $\beta_{eff}\cdot\alpha_{handle}$ is given by $(Rg/L)(6\pi\eta A_0E)$. Neglecting constant coefficients, the product $\beta_{eff}\cdot\alpha_{handle}$ is proportional to the dimensionless factor Rg/L.

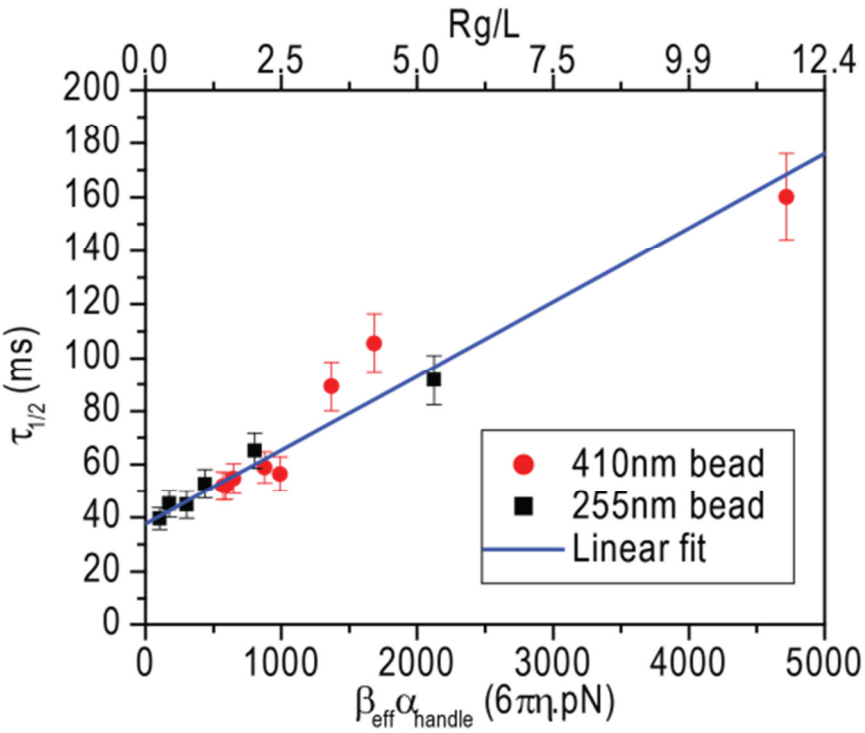

Figure 4.4: Coexistence lifetime $\tau_{1/2}$ is linear to the dimensionless factor Rg/L and the product of effective drag coefficient for the microsphere and stiffness of DNA handle.

As shown in Fig. 4.4, the measured values of $\tau_{1/2}$ collapse onto a single curve when plotted as a function of $\beta_{\text{eff}} \cdot \alpha_{\text{handle}}$. This indicates that the dimensionless number Rg/L determines the extent to which the coexistence lifetime is perturbed by the measurement system (when other parameters of the measurement system are held fixed). The least-squares linear fit to the data is $\tau_{1/2} = (37.7 \pm 2.1)$ ms + $(Rg/L)(11.1 \pm 1.0)$ ms. Extrapolating to $Rg/L = 0$ gives an asymptotic hairpin coexistence time of $\tau_{1/2} = 38 \pm 2$ ms.

Previous results indicated that while long handles result in the most accurate measurement of the intrinsic transition rate of a bio-molecule [103], short handles provide higher resolution for reconstructing energy landscapes [106]. Our experiments indicate that when measuring the transition kinetics, the radius of the microsphere sets the effective scale for the handle length, and that the more reliable measurement of the transition rate is obtained when L>>R. Smaller microspheres as well as longer handles can be used to reduce the artificial influence of the measurement system on the transition kinetics. This limit appears to represent a minimum perturbation to the hairpin transition kinetics by the measurement system. However, even in this limit we must allow for the possibility that other effects, such as drag due to the handles themselves, are causing the observed transition rate to deviate from the intrinsic rate.

4.4 Conclusion

We have measured the transition lifetime for a two-state hairpin using a range of handle lengths and two sizes of microsphere The observed transition rate did not

exhibit a simple functional dependence on the tether length, the effective drag coefficient of the microsphere, or on the characteristic time scales of the optical trapping assay. The perturbation to the intrinsic transition rate is a function of the dimensionless parameter Rg/L. This result is consistent with the assumption that drag associated with the microsphere is the dominant factor in slowing down the transition kinetics. The perturbation to the intrinsic transition rate increases with increasing R (which increases the drag coefficient on the microsphere) and decreases with increasing L (which weakens the coupling between the microsphere and the hairpin). However, we are not aware of an argument from first principles which would explain the functional dependence on Rg/L. We believe that further theoretical work may elucidate the details of these mechanisms.

Chapter 5: Conclusion and Perspective

In this thesis, we develop methods for force and torque measurement and apply them to various single-molecule experiments. Using optical traps, we study the unfolding pathways of CCR5 mRNA, DNA mismatch energy, DNA G-quadruplex disruption, and transcription dynamics of RNA polymerase. On the other hand, we construct optical torque wrench and fabricate birefringent quartz cylinder to achieve simultaneous force and torque control and measurement. This is applied to measure mechanical properties of twisted and stretched DNA. Furthermore, we study nucleosome unwrapping under tension and torsion and find that torsional effect is crucial towards understanding the biological processes.

Recently there are more researches intending to elucidate the role torsion plays in biological system. A natural extension of this thesis is to study transcription of polymerase through nucleosome under torsion, which may give us insight of underlying mechanism. We expect the methodology developed in this thesis can serve as basis for future study and lead to more fruitful results.

Appendix A: G-quadruplex Disruption With DFS

A.1 Experimental Details

Double-stranded DNA handles were generated by PCR with digoxigenin and biotin labeled primers and digested with BtgI or BstXI enzymes to produce 4-base sticky ends. Data was taken using two different handle configurations with total lengths 3716 or 2432 base pairs. A control hairpin studied previously [17] was synthesized with sequence *gagtcaacgtctggatcctgttttcaggatccagacgttgactc*. The quadruplex was synthesized with sequence $(acaggggtgtgggg)_2aca$, identical to that used in previously reported results [27]. The quadruplex and control hairpin were ligated between the handles and gel purified. The surface of the sample chamber was coated with blotting buffer to prevent interactions with the surface. Final buffer conditions were 100 mM KCl, 2 mM EDTA, 10 mM Tris buffer (pH 8.0), 0.02% Tween 20, and oxygen-scavenging solution (721 μg/ml glucose oxidase, 144 μg/ml catalase, and 3.9 mg/ml glucose) which increased the lifetime of the samples under exposure to the trapping beam. Data was collected on a single-beam optical trap at 10 kHz using an 8-pole 5 kHz Bessel filter

To provide a reliable force loading rate, feedback to the stage position was used to maintain the bead at a fixed position relative to the optical trap as the optical power was increased at a constant rate using an acousto-optic modulator. For each individual scan the initial force, the maximum accessible force, and the force of the observed disruption, if any, were recorded.

Each sample was scanned repeatedly until the tether broke or the sample stopped showing any further disruptions. Between scans the sample was brought to a

relaxed state at zero force for 5 seconds to allow the quadruplex time to refold. In order to ensure that the disruptions in our statistical sample came from quadruplexes that had formed under identical circumstances, we discarded the first disruption from each molecule.

In order to verify the force and displacement calibration of our measurements and confirm slide-to-slide consistency, each sample chamber was prepared so that roughly half of the tethers had the G4-quadruplex molecule and the remainder had the control hairpin. The type of molecule linked to any given tether is easily determined from the nature of the disruptions observed. Measurements of the control hairpin yielded opening size 17.5 nm with standard deviation 1.7 nm, and disruption force of approximately 13 pN, in agreement with previously reported values [15]. Typical scans of the control hairpin and quadruplex are shown in Figure A.1.

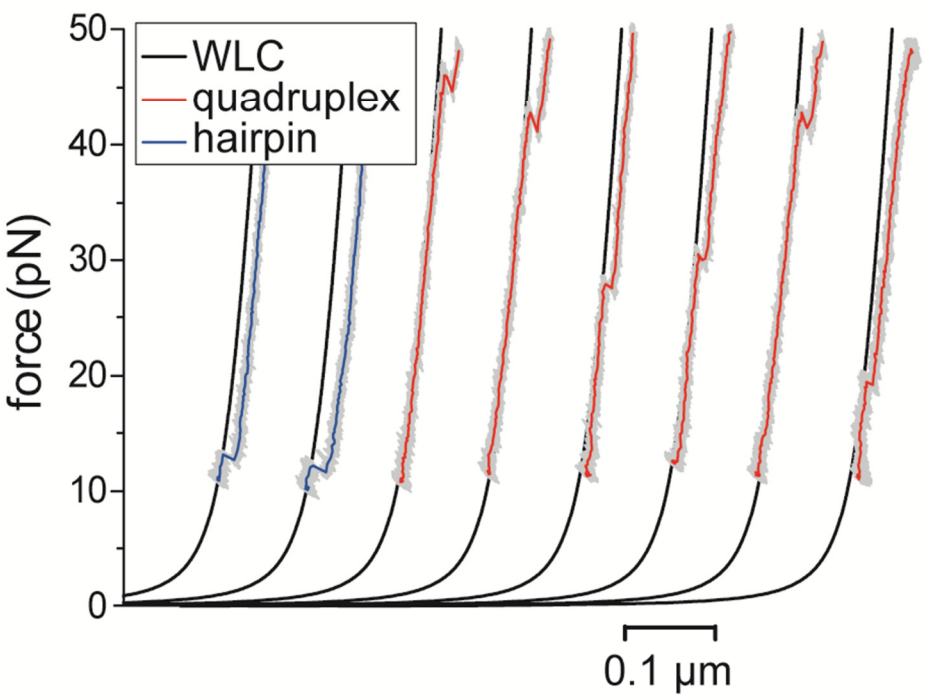

Figure A.1: Raw data scans at 24 pN/s for quadruplex (red) and control hairpin (blue) overlaid on a worm-like chain model with persistence length 41 nm, stretch modulus 1277 pN, and contour length per base of 0.338 nm. Each scan was preceded by a relaxation period at zero force for 5 s.

We expect the 25-mer G4-quadruplex to release about 21 bases after accounting for the width of the quadruplex structure. Opening distances were converted to the number of single-stranded bases using a worm-like chain model [13] for the single-stranded DNA with persistence length 1.25 nm, contour length of 0.625 nm/base, and neglecting enthalpic contributions. We measured an opening size of 20.3 bases, standard deviation 2.5 bases, shown in Figure A.2. To assure that each tether analyzed had a single-molecule attachment we excluded tethers that failed to produce the expected low-force stretch curve or that exhibited asymmetry for *x* and *y* stretching. To exclude improperly folded molecules from the sample we excluded

disruptions for which the number of bases released was more than 2 standard deviations from the mean value or for which multiple disruptions were observed on a single scan.

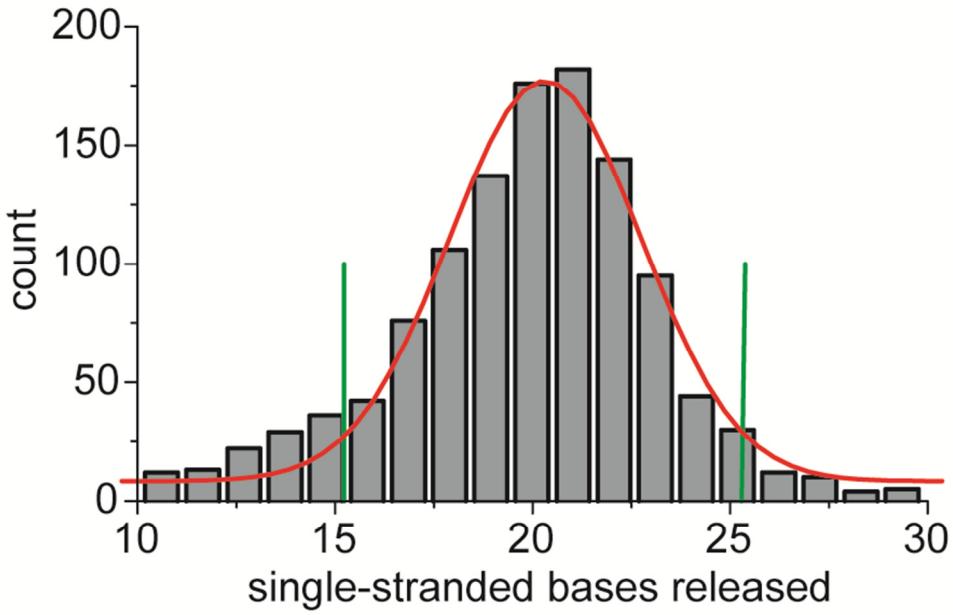

Figure A.2: Opening distance for the G4-quadruplex with mean 20.3 single-stranded bases released and standard deviation 2.5 bases. The data was filtered two standard deviations from the mean (green boundaries).

A.2 DFS Fitting Details

The Dudko models are preferred in principle, since they correctly take into account the dependence of the transition state position on force and avoid some of the inconsistencies which have been encountered in the application of the Evans model, including underestimation of d and overestimation of k [32,34]. In addition, the Bayesian information criterion, that likelihood should increase by $\ln(N)/2$ for each additional fitting parameter, is satisfied for the Dudko models, which include G_1 and G_2 as fitting parameters [112].

Fitting the distributions of disruption force in detail, rather than simply analyzing the most likely or mean disruption force as a function of loading rate, gives a more exhaustive comparison of data with theory, and allows the overlapping distributions associated with the parallel and anti-parallel conformations to be identified.

A.3 Further Discussions

The Dudko models indicate that the height of the energy barrier is approximately 10 k_BT. An applied force will tilt the energy landscape, adding a term $-Fx$ to the effective energy as a function of the opening distance x, and disruption typically occurs when the force cancels the slope of the native landscape. The quadruplex has a high disruption force because of the short distance and steep slope to the principal barrier, despite its modest height. However, DFS measurements will not be sensitive to one or more secondary barriers beyond d with a more shallow energy slope [113].

The DFS measurements provide an interesting contrast with previous results by Yu et al., in which the energy of the fully unfolded state of G-quadruplex was measured with respect to the folded state. In Figure 1.11 we present a model of the energy landscape of the antisymmetric conformation which consists of the primary barrier determined by our DFS analysis followed by a more shallow slope which connects the primary barrier to the energy of the fully unfolded state, as measured by Yu et al. The combination of the two measurements defines the broad properties of the energy landscape for disruption: a sharp rise in energy for initial disruption of the structure (2.5 kcal/mol for each base released), followed by a more gradual increase of energy as the remaining portion of the structure is disrupted (an average of 0.9 kcal/mole for each additional base released). Qualitatively similar results are obtained for the parallel conformation. This landscape implies a highly cooperative unfolding process, where a disproportionate portion of the binding energy comes from the initial stages of disruption.

Full knowledge of the configuration of the energy landscape can be related to the resistance of the system to different disruption modes, including disruption by progressive enzymes, The probability of occupying a state of energy H is $\exp(-H/k_{\mathrm{B}}T)$ so the quadruplex is much more likely to reach the transition state than the fully open state as a result of thermal excitation. This implies that a processive enzyme that would otherwise be stalled by the formidable disruption force could take advantage of thermal fluctuations to reach the transition state, then progress more easily along the more shallow regime of the energy landscape.

The results of Table A.1 are comparable with those reported in a prior AFM study of a bi-molecular form of a different G4-quadruplex sequence, though the previous study assumed a single unknown conformation type [114]. The results reported in the AFM study appear to be consistent with the parallel conformation (see Figure A.3). The high precision of the optical trap experiments made it possible to resolve the two distinct conformations of the ILPR G-quadruplex sequence identified by Yu et al. This facilitated comparisons between the corresponding barrier height and final state energies.

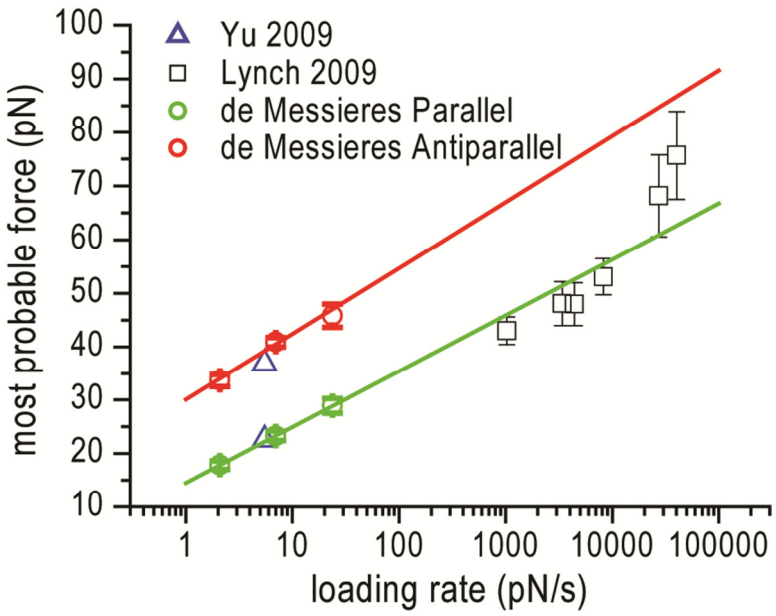

Figure A.3: Comparison of most probable force from our data, Yu, and Lynch. The alignment of our parallel data points suggests that Lynch was fitting to a parallel form. Our data points and uncertainties are generated from the global fit values determined in Table A.1.

v	$\ln(L_m)/L_0$	w	d_p(Å)	d_a(Å)	$\log k_p(s^{-1})$	$\log k_a(s^{-1})$	G_p (kCal/mol)	G_a (kCal/mol)
1	0	0.33 ± 0.05	6.8 ± 0.9	6.1 ± 0.9	-1.7 ± 0.2	-2.7 ± 0.3	-	-
2/3	+2.2 ± 1.0	0.29 ± 0.05	13 ± 3	10 ± 2	-2.4 ± 0.3	-3.3 ± 0.5	5.3 ± 0.4	5.1 ± 1.2
1/2	+2.3 ± 0.9	0.31 ± 0.09	16 ± 3	14 ± 4	-2.7 ± 0.3	-4.0 ± 0.8	5.5 ± 0.5	7 ± 2

Table A.1: Summary of global maximum-likelihood fits for different values of v. $\ln(L_m)/L_0$ indicates the log of the maximum-likelihood score relative to the result for $v = 1$, normalized by $L_0 = \ln(N)/2$ where $N = 1014$ data points. Uncertainties were determined by bootstrapping. Weight (w) indicates the percentage allocated to the parallel conformation (subscript p) while the antiparallel conformation (subscript a) is allocated percentage ($1–w$).

Bibliography

[1] C. Bustamante, In singulo biochemistry: When less is more, Annu. Rev. Biochem. 77 (2008) 45–50.

[2] N.G. Walter, C.Y. Huang, A.J. Manzo, M.A. Sobhy, Do-it-yourself guide: how to use the modern single-molecule toolkit, Nat. Methods. 5 (2008) 475–489.

[3] C. Joo, H. Balci, Y. Ishitsuka, C. Buranachai, T. Ha, Advances in Single-Molecule Fluorescence Methods for Molecular Biology, Annu. Rev. Biochem. 77 (2008) 51–76.

[4] K.C. Neuman, A. Nagy, Single-molecule force spectroscopy: optical tweezers, magnetic tweezers and atomic force microscopy, Nat. Methods. 5 (2008) 491–505.

[5] A. Ashkin, ACCELERATION AND TRAPPING OF PARTICLES BY RADIATION PRESSURE, Phys. Rev. Lett. 24 (1970) 156–&.

[6] A. Ashkin, J.M. Dziedzic, J.E. Bjorkholm, S. Chu, OBSERVATION OF A SINGLE-BEAM GRADIENT FORCE OPTICAL TRAP FOR DIELECTRIC PARTICLES, Opt. Lett. 11 (1986) 288–290.

[7] K. Svoboda, S.M. Block, BIOLOGICAL APPLICATIONS OF OPTICAL FORCES, Annu. Rev. Biophys. Biomol. Struct. 23 (1994) 247–285.

[8] T.A. Nieminen, V.L.Y. Loke, A.B. Stilgoe, G. Knoner, A.M. Branczyk, N.R. Heckenberg, et al., Optical tweezers computational toolbox, J. Opt. -Pure Appl. Opt. 9 (2007) S196–S203.

[9] K.C. Neuman, S.M. Block, Optical trapping, Rev. Sci. Instrum. 75 (2004) 2787–2809.

[10] K.C. Neuman, E.A. Abbondanzieri, S.M. Block, Measurement of the effective focal shift in an optical trap, Opt Lett. 30 (2005) 1318–1320.

[11] J.R. Moffitt, Y.R. Chemla, S.B. Smith, C. Bustamante, Recent advances in optical tweezers, Annu. Rev. Biochem. 77 (2008) 205–228.

[12] C. Deufel, M.D. Wang, Detection of Forces and Displacements along the Axial Direction in an Optical Trap, Biophys. J. 90 (2006) 657–667.

[13] J.F. Marko, E.D. Siggia, Stretching DNA, Macromolecules. 28 (1995) 8759–8770.

[14] M.T. Woodside, P.C. Anthony, W.M. Behnke-Parks, K. Larizadeh, D. Herschlag, S.M. Block, Direct measurement of the full, sequence-dependent folding landscape of a nucleic acid, Science. 314 (2006) 1001–1004.

[15] M.T. Woodside, W.M. Behnke-Parks, K. Larizadeh, K. Travers, D. Herschlag, S.M. Block, Nanomechanical measurements of the sequence-dependent folding landscapes of single nucleic acid hairpins, Proc. Natl. Acad. Sci. U. S. A. 103 (2006) 6190–6195.

[16] A. La Porta, N.A. Denesyuk, M. de Messieres, Optimal reconstruction of the folding landscape using differential energy surface analysis, Phys. Rev. E. 87 (2013) 032716.

[17] M. de Messieres, B. Brawn-Cinani, A. La Porta, Measuring the Folding Landscape of a Harmonically Constrained Biopolymer, Biophys. J. 100 (2011) 2736–2744.

[18] M. de Messieres, J.-C. Chang, B. Brawn-Cinani, A. La Porta, Single-Molecule Study of G-Quadruplex Disruption Using Dynamic Force Spectroscopy, Phys. Rev. Lett. 109 (2012) 058101.

[19] M. Gellert, M.N. Lipsett, D.R. Davies, HELIX FORMATION BY GUANYLIC ACID, Proc. Natl. Acad. Sci. U. S. A. 48 (1962) 2013–2018.

[20] D.E. Gilbert, J. Feigon, Multistranded DNA structures, Curr. Opin. Struct. Biol. 9 (1999) 305–314.

[21] J.L. Huppert, Four-stranded nucleic acids: structure, function and targeting of G-quadruplexes, Chem. Soc. Rev. 37 (2008) 1375–1384.

[22] H.J. Lipps, D. Rhodes, G-quadruplex structures: in vivo evidence and function, Trends Cell Biol. 19 (2009) 414–422.

[23] J.L. Huppert, S. Balasubramanian, G-quadruplexes in promoters throughout the human genome, Nucleic Acids Res. 35 (2007) 406–413.

[24] S. Balasubramanian, L.H. Hurley, S. Neidle, Targeting G-quadruplexes in gene promoters: a novel anticancer strategy?, Nat. Rev. Drug Discov. 10 (2011) 261–275.

[25] S. Neidle, G. Parkinson, Telomere maintenance as a target for anticancer drug discovery, Nat. Rev. Drug Discov. 1 (2002) 383–393.

[26] S. Dhakal, J.D. Schonhoft, D. Koirala, Z. Yu, S. Basu, H. Mao, Coexistence of an ILPR i-Motif and a Partially Folded Structure with Comparable Mechanical Stability Revealed at the Single-Molecule Level, J. Am. Chem. Soc. 132 (2010) 8991–8997.

[27] Z.B. Yu, J.D. Schonhoft, S. Dhakal, R. Bajracharya, R. Hegde, S. Basu, et al., ILPR G-Quadruplexes Formed in Seconds Demonstrate High Mechanical Stabilities, J. Am. Chem. Soc. 131 (2009) 1876–1882.

[28] J.D. Schonhoft, A. Das, F. Achamyeleh, S. Samdani, A. Sewell, H. Mao, et al., ILPR repeats adopt diverse G-quadruplex conformations that determine insulin binding, Biopolymers. 93 (2010) 21–31.

[29] E. Evans, K. Ritchie, Dynamic strength of molecular adhesion bonds, Biophys. J. 72 (1997) 1541–1555.

[30] E. Evans, Probing the relation between force - Lifetime - and chemistry in single molecular bonds, Annu. Rev. Biophys. Biomol. Struct. 30 (2001) 105–128.

[31] S.J. Koch, M.D. Wang, Dynamic force spectroscopy of protein-DNA interactions by unzipping DNA, Phys. Rev. Lett. 91 (2003).

[32] G. Hummer, A. Szabo, Kinetics from Nonequilibrium Single-Molecule Pulling Experiments, Biophys. J. 85 (2003) 5–15.

[33] O.K. Dudko, A.E. Filippov, J. Klafter, M. Urbakh, Beyond the conventional description of dynamic force spectroscopy of adhesion bonds, Proc. Natl. Acad. Sci. U. S. A. 100 (2003) 11378–11381.

[34] O.K. Dudko, G. Hummer, A. Szabo, Intrinsic Rates and Activation Free Energies from Single-Molecule Pulling Experiments, Phys. Rev. Lett. 96 (2006) 108101.

[35] M.H. Larson, R. Landick, S.M. Block, Single-Molecule Studies of RNA Polymerase: One Singular Sensation, Every Little Step It Takes, Mol. Cell. 41 (2011) 249–262.

[36] C. Bustamante, W. Cheng, Y.X. Mejia, Revisiting the Central Dogma One Molecule at a Time, Cell. 144 (2011) 480–497.

[37] K.M. Herbert, W.J. Greenleaf, S.M. Block, Single-Molecule Studies of RNA Polymerase: Motoring Along, Annu. Rev. Biochem. 77 (2008) 149–176.

[38] T.T. Perkins, Optical traps for single molecule biophysics: a primer, Laser Photonics Rev. 3 (2009) 203–220.

[39] I. Tinoco, R.L. Gonzalez, Biological mechanisms, one molecule at a time, Genes Dev. 25 (2011) 1205–1231.

[40] K.C. Neuman, E.A. Abbondanzieri, R. Landick, J. Gelles, S.M. Block, Ubiquitous transcriptional pausing is independent of RNA polymerase backtracking, Cell. 115 (2003) 437–447.

[41] K.M. Herbert, A. La Porta, B.J. Wong, R.A. Mooney, K.C. Neuman, R. Landick, et al., Sequence-resolved detecton of pausing by single RNA polymerase molecules, Cell. 125 (2006) 1083–1094.

[42] V.R. Tadigotla, D. O'Maoileidigh, A.M. Sengupta, V. Epshtein, R.H. Ebright, E. Nudler, et al., Thermodynamic and kinetic modeling of transcriptional pausing, Proc. Natl. Acad. Sci. U. S. A. 103 (2006) 4439–4444.

[43] J. Zhou, K.S. Ha, A. LaÂ Porta, R. Landick, S.M. Block, Applied Force Provides Insight into Transcriptional Pausing and Its Modulation by Transcription Factor NusA, Mol. Cell. 44 (2011) 635–646.

[44] C. Hodges, L. Bintu, L. Lubkowska, M. Kashlev, C. Bustamante, Nucleosomal Fluctuations Govern the Transcription Dynamics of RNA Polymerase II, Science. 325 (2009) 626–628.

[45] L. Bintu, M. Kopaczynska, C. Hodges, L. Lubkowska, M. Kashlev, C. Bustamante, The elongation rate of RNA polymerase determines the fate of transcribed nucleosomes, Nat. Struct. Mol. Biol. 18 (2011) 1394–1399.

[46] L. Bintu, T. Ishibashi, M. Dangkulwanich, Y.-Y. Wu, L. Lubkowska, M. Kashlev, et al., Nucleosomal Elements that Control the Topography of the Barrier to Transcription, Cell. 151 (2012) 738–749.

[47] J. Ma, L. Bai, M.D. Wang, Transcription Under Torsion, Science. 340 (2013) 1580–1583.

[48] S. Toyabe, T. Watanabe-Nakayama, T. Okamoto, S. Kudo, E. Muneyuki, Thermodynamic efficiency and mechanochemical coupling of F1-ATPase, Proc. Natl. Acad. Sci. 108 (2011) 17951–17956.

[49] J. Xing, F. Bai, R. Berry, G. Oster, Torque–speed relationship of the bacterial flagellar motor, Proc. Natl. Acad. Sci. U. S. A. 103 (2006) 1260–1265.

[50] X. Chen, H.C. Berg, Solvent-Isotope and pH Effects on Flagellar Rotation in Escherichia coli, Biophys. J. 78 (2000) 2280–2284.

[51] J. Rybczynski, U. Ebels, M. Giersig, Large-scale, 2D arrays of magnetic nanoparticles, Colloids Surfaces Physicochem. Eng. Asp. 219 (2003) 1–6.

[52] A. Kosiorek, W. Kandulski, H. Glaczynska, M. Giersig, Fabrication of Nanoscale Rings, Dots, and Rods by Combining Shadow Nanosphere Lithography and Annealed Polystyrene Nanosphere Masks, Small. 1 (2005) 439–444.

[53] A. La Porta, M.D. Wang, Optical torque wrench: Angular trapping, rotation, and torque detection of quartz microparticles, Phys. Rev. Lett. 92 (2004) 190801.

[54] A.I. Bishop, T.A. Nieminen, N.R. Heckenberg, H. Rubinsztein-Dunlop, Optical application and measurement of torque on microparticles of isotropic nonabsorbing material, Phys. Rev. 68 (2003) 033802.

[55] S.H. Simpson, S. Hanna, Application of the discrete dipole approximation to optical trapping calculations of inhomogeneous and anisotropic particles, Opt Express. 19 (2011) 16526–16541.

[56] S.H. Simpson, S. Hanna, Computational study of the optical trapping of ellipsoidal particles, Phys. Rev. 84 (2011) 053808.

[57] S.H. Simpson, S. Hanna, Optical trapping of microrods: variation with size and refractive index, J Opt Soc Am. 28 (2011) 850–858.

[58] L. Oroszi, P. Galajda, H. Kirei, S. Bottka, P. Ormos, Direct measurement of torque in an optical trap and its application to double-strand DNA, Phys. Rev. Lett. 97 (2006).

[59] B. Gutiérrez-Medina, J.O.L. Andreasson, W.J. Greenleaf, A. LaPorta, S.M. Block, G.W. Nils, Chapter 15 - An Optical Apparatus for Rotation and Trapping, in: Methods Enzymol., Academic Press, 2010: pp. 377–404.

[60] C. Deufel, S. Forth, C.R. Simmons, S. Dejgosha, M.D. Wang, Nanofabricated quartz cylinders for angular trapping: DNA supercoiling torque detection - supp, Nat. Methods. 4 (2007) 223–225.

[61] Z. Huang, F. Pedaci, M. van Oene, M.J. Wiggin, N.H. Dekker, Electron Beam Fabrication of Birefringent Microcylinders, ACS Nano. 5 (2011) 1418–1427.

[62] F. Pedaci, Z. Huang, M. van Oene, N.H. Dekker, Calibration of the optical torque wrench, Opt Express. 20 (2012) 3787–3802.

[63] M.M. Tirado, J.G. de la Torre, Rotational dynamics of rigid, symmetric top macromolecules. Application to circular cylinders, J. Chem. Phys. 73 (1980) 1986–1993.

[64] J.F. Marko, Torque and dynamics of linking number relaxation in stretched supercoiled DNA, Phys. Rev. E. 76 (2007) 021926.

[65] J.F. Marko, Micromechanics of Single Supercoiled DNA Molecules, in: C.J. Benham, S. Harvey, W.K. Olson, D.W. Sumners, D. Swigon (Eds.), Math. DNA Struct. Funct. Interactions, Springer New York, 2009: pp. 225–249.

[66] F. Mosconi, J.F. Allemand, D. Bensimon, V. Croquette, Measurement of the Torque on a Single Stretched and Twisted DNA Using Magnetic Tweezers, Phys. Rev. Lett. 102 (2009) 078301.

[67] T.R. Strick, J.F. Allemand, D. Bensimon, A. Bensimon, V. Croquette, The Elasticity of a Single Supercoiled DNA Molecule, Science. 271 (1996) 1835–1837.

[68] M.Y. Sheinin, S. Forth, J.F. Marko, M.D. Wang, Underwound DNA under Tension: Structure, Elasticity, and Sequence-Dependent Behaviors, Phys. Rev. Lett. 107 (2011) 108102.

[69] S. Forth, C. Deufel, M.Y. Sheinin, B. Daniels, J.P. Sethna, M.D. Wang, Abrupt buckling transition observed during the plectoneme formation of individual DNA molecules, Phys. Rev. Lett. 100 (2008).

[70] M.Y. Sheinin, M.D. Wang, Twist-stretch coupling and phase transition during DNA supercoiling, Phys. Chem. Chem. Phys. 11 (2009) 4800–4803.

[71] S. Forth, M.Y. Sheinin, J. Inman, M.D. Wang, Torque Measurement at the Single-Molecule Level, Annu. Rev. Biophys. 42 (2013) 583–604.

[72] K. Luger, A.W. Mader, R.K. Richmond, D.F. Sargent, T.J. Richmond, Crystal structure of the nucleosome core particle at 2.8[thinsp]A resolution, Nature. 389 (1997) 251–260.

[73] W. Humphrey, A. Dalke, K. Schulten, VMD: Visual molecular dynamics, J. Mol. Graph. 14 (1996) 33–38.

[74] F.T. Chien, J. van Noort, 10 Years of Tension on Chromatin: Results from Single Molecule Force Spectroscopy, Curr. Pharm. Biotechnol. 10 (2009) 474–485.

[75] C. Lavelle, J.-M. Victor, J. Zlatanova, Chromatin Fiber Dynamics under Tension and Torsion, Int. J. Mol. Sci. 11 (2010) 1557–1579.

[76] J. Bednar, S. Dimitrov, Chromatin under mechanical stress: from single 30 nm fibers to single nucleosomes, FEBS J. 278 (2011) 2231–2243.

[77] J.L. Killian, M. Li, M.Y. Sheinin, M.D. Wang, Recent advances in single molecule studies of nucleosomes, Curr. Opin. Struct. Biol. 22 (2012) 80–87.

[78] J.S. Choy, T.-H. Lee, Structural dynamics of nucleosomes at single-molecule resolution, Trends Biochem. Sci. 37 (2012) 425–435.

[79] A.H. Mack, D.J. Schlingman, R.P. Ilagan, L. Regan, S.G.J. Mochrie, Kinetics and Thermodynamics of Phenotype: Unwinding and Rewinding the Nucleosome, J. Mol. Biol. 423 (2012) 687–701.

[80] B.D. Brower-Toland, C.L. Smith, R.C. Yeh, J.T. Lis, C.L. Peterson, M.D. Wang, Mechanical disruption of individual nucleosomes reveals a reversible multistage release of DNA, Proc. Natl. Acad. Sci. U. S. A. 99 (2002) 1960–1965.

[81] S. Mihardja, A.J. Spakowitz, Y. Zhang, C. Bustamante, Effect of force on mononucleosomal dynamics, Proc. Natl. Acad. Sci. 103 (2006) 15871–15876.

[82] P. Prinsen, H. Schiessel, Nucleosome stability and accessibility of its DNA to proteins, Biochimie. 92 (2010) 1722–1728.

[83] I.M. Kulić, H. Schiessel, DNA Spools under Tension, Phys. Rev. Lett. 92 (2004) 228101.

[84] R. Blossey, H. Schiessel, The dynamics of the nucleosome: thermal effects, external forces and ATP, FEBS J. 278 (2011) 3619–3632.

[85] A. Bancaud, N. Conde e Silva, M. Barbi, G. Wagner, J.-F. Allemand, J. Mozziconacci, et al., Structural plasticity of single chromatin fibers revealed by torsional manipulation, Nat Struct Mol Biol. 13 (2006) 444–450.

[86] A. Bancaud, G. Wagner, N. Conde e Silva, C. Lavelle, H. Wong, J. Mozziconacci, et al., Nucleosome Chiral Transition under Positive Torsional Stress in Single Chromatin Fibers, Mol. Cell. 27 (2007) 135–147.

[87] V.M. Studitsky, Preparation and Analysis of Positioned Nucleosomes, in: Chromatin Protoc., 1999: pp. 17–26.

[88] A. Thåström, P.T. Lowary, J. Widom, Measurement of histone-DNA interaction free energy in nucleosomes, Methods. 33 (2004) 33–44.

[89] M. Kruithof, F.-T. Chien, A. Routh, C. Logie, D. Rhodes, J. van Noort, Single-molecule force spectroscopy reveals a highly compliant helical folding for the 30-nm chromatin fiber, Nat. Struct. Mol. Biol. 16 (2009) 534–540.

[90] M. Kruithof, J. van Noort, Hidden Markov Analysis of Nucleosome Unwrapping Under Force, Biophys. J. 96 (2009) 3708–3715.

[91] L.H. Pope, M.L. Bennink, J. Greve, Optical tweezers stretching of chromatin, J. Muscle Res. Cell Motil. 23 (2002) 397–407.

[92] L.H. Pope, M.L. Bennink, K.A. van Leijenhorst-Groener, D. Nikova, J. Greve, J.F. Marko, Single Chromatin Fiber Stretching Reveals Physically Distinct Populations of Disassembly Events, Biophys. J. 88 (2005) 3572–3583.

[93] L.F. Liu, J.C. Wang, Supercoiling of the DNA template during transcription, Proc. Natl. Acad. Sci. 84 (1987) 7024–7027.

[94] F. Kouzine, S. Sanford, Z. Elisha-Feil, D. Levens, The functional response of upstream DNA to dynamic supercoiling in vivo, Nat. Struct. Mol. Biol. 15 (2008) 146–154.

[95] L. Baranello, D. Levens, A. Gupta, F. Kouzine, The importance of being supercoiled: How DNA mechanics regulate dynamic processes, Biochim. Biophys. Acta BBA - Gene Regul. Mech. 1819 (2012) 632–638.

[96] F. Kouzine, A. Gupta, L. Baranello, D. Wojtowicz, K. Ben-Aissa, J. Liu, et al., Transcription-dependent dynamic supercoiling is a short-range genomic force, Nat. Struct. Mol. Biol. 20 (2013) 396–403.

[97] J. Zlatanova, T.C. Bishop, J.-M. Victor, V. Jackson, K. van Holde, The Nucleosome Family: Dynamic and Growing, Struct. Lond. Engl. 1993. 17 (2009) 160–171.

[98] T.A. Hagerman, Q. Fu, B. Molinié, J. Denvir, S. Lindsay, P.T. Georgel, Chromatin Stability at Low Concentration Depends on Histone Octamer Saturation Levels, Biophys. J. 96 (2009) 1944–1951.

[99] M.L. Kireeva, B. Hancock, G.H. Cremona, W. Walter, V.M. Studitsky, M. Kashlev, Nature of the Nucleosomal Barrier to RNA Polymerase II, Mol. Cell. 18 (2005) 97–108.

[100] O.I.S. Kulaeva, Mechanism of histone survival during transcription by RNA polymerase II, Transcription. 1 (2010) 85–88.

[101] J.-C. Chang, M. de Messieres, A. La Porta, Effect of handle length and microsphere size on transition kinetics in single-molecule experiments, Phys. Rev. E. 87 (2013) 012721.

[102] W.J. Greenleaf, M.T. Woodside, E.A. Abbondanzieri, S.M. Block, Passive all-optical force clamp for high-resolution laser trapping, Phys. Rev. Lett. 95 (2005).

[103] M. Manosas, J.D. Wen, P.T.X. Li, S.B. Smith, C. Bustamante, I. Tinoco, et al., Force Unfolding Kinetics of RNA using Optical Tweezers. II. Modeling Experiments, Biophys. J. 92 (2007) 3010–3021.

[104] J.-D. Wen, M. Manosas, P.T.X. Li, S.B. Smith, C. Bustamante, F. Ritort, et al., Force Unfolding Kinetics of RNA Using Optical Tweezers. I. Effects of Experimental Variables on Measured Results, Biophys. J. 92 (2007) 2996–3009.

[105] N. Forns, S. de Lorenzo, M. Manosas, K. Hayashi, J.M. Huguet, F. Ritort, Improving Signal/Noise Resolution in Single-Molecule Experiments Using Molecular Constructs with Short Handles, Biophys. J. 100 (2011) 1765–1774.

[106] C. Hyeon, G. Morrison, D. Thirumalai, Force-dependent hopping rates of RNA hairpins can be estimated from accurate measurement of the folding landscapes, Proc Nat Acad Sci USA. 105 (2008) 9604–9609.

[107] M.P. Landry, P.M. McCall, Z. Qi, Y.R. Chemla, Characterization of Photoactivated Singlet Oxygen Damage in Single-Molecule Optical Trap Experiments, Biophys. J. 97 (2009) 2128–2136.

[108] Y. Gao, G. Sirinakis, Y. Zhang, Highly Anisotropic Stability and Folding Kinetics of a Single Coiled Coil Protein under Mechanical Tension, J. Am. Chem. Soc. 133 (2011) 12749–12757.

[109] E. Schäffer, S.F. Nørrelykke, J. Howard, Surface Forces and Drag Coefficients of Microspheres near a Plane Surface Measured with Optical Tweezers, Langmuir. 23 (2007) 3654–3665.

[110] R.G. Cox, The motion of long slender bodies in a viscous fluid Part 1. General theory, J. Fluid Mech. 44 (1970) 791–810.

[111] M. Manosas, F. Ritort, Thermodynamic and Kinetic Aspects of RNA Pulling Experiments, Biophys. J. 88 (2005) 3224–3242.

[112] O.K. Dudko, J. Mathé, A. Szabo, A. Meller, G. Hummer, Extracting Kinetics from Single-Molecule Force Spectroscopy: Nanopore Unzipping of DNA Hairpins, 92 (2007) 4188–4195.

[113] C. Hyeon, D. Thirumalai, Measuring the energy landscape roughness and the transition state location of biomolecules using single molecule mechanical unfolding experiments, J. Phys. Condens. Matter. 19 (2007) 113101.

[114] S. Lynch, H. Baker, S. Byker, D. Zhou, K. Sinniah, Single Molecule Force Spectroscopy on G-Quadruplex DNA, Chem. – Eur. J. 15 (2009) 8113–8116.